MEASURING SOLAR NEUTRINO FLUX IN THE SNO+ PURE SCINTILLATOR PHASE

Eric Marzec

A DISSERTATION

in

Physics and Astronomy

Presented to the Faculties of the University of Pennsylvania

in

Partial Fulfillment of the Requirements for the Degree of

Doctor of Philosophy

2018

Supervisor of Dissertation	**Graduate Group Chairperson**
J.R. Klein	J.R. Klein
Professor, Physics and Astronomy	Professor, Physics and Astronomy

Dissertation Comittee:

Joe Kroll, Professor, Physics and Astronomy

Christopher Mauger, Professor, Physics and Astronomy

Justin Khoury, Professor, Physics and Astronomy

Doc 4, Professor, Physics and Astronomy

Doc 5, Professor, Physics and Astronomy

Doc 6, Professor, Physics and Astronomy

MEASURING SOLAR NEUTRINO FLUX IN THE SNO+ PURE SCINTILLATOR PHASE

Acknowledgements

ABSTRACT

MEASURING SOLAR NEUTRINO FLUX IN THE SNO+ PURE SCINTILLATOR PHASE

Eric Marzec

J.R. Klein

Described here is a measurement of the solar neutrino flux as measured by SNO+.

Contents

List of Tables

List of Figures

Chapter 1

Introduction

Predictions and measurements associated with solar neutrinos, among other sources, has provided strong evidence that neutrinos are massive and undergo flavor oscillations. The neutrino occupies a fairly unique role in modern particle physics. Despite being ubiquitous, created by a wide variety of physical phenomena, many of its fundamental properties remain unknown. The core reason for this uncertainty is that the neutrino interacts extremely rarely with standard matter, meaning that a wide variety of techniques used is difficult to study.

Predictions regarding the neutrino flux produced by the sun has been developed since the 19XX (**?**). Many refinements to these original predictions have been made over the years as our understanding of the Sun and of nuclear reactions have improved (**? ? ?**). Simultaneous with improvements in prediction, methods for detecting neutrinos improved as well. The first experiment capable of successfully detecting neutrinos from the Sun was the Homestake Neutrino Experiment.

Numerous experiments studying neutrinos from a wide variety of sources have contributed over the last century to our current understanding of neutrino properties. These experiment have provided near conclusive evidence of neutrino flavor oscillations, which in turn requires that the neutrino have mass, and that lepton flavor is not a fundamental symmetry of the universe.

Chapter **??** provides a basic introduction to the physics associated with neutrinos, neutrino interactions, and neutrino mixing. These physical ideas are applied to solar physics and solar neutrinos in Chapter **??** to develop predictions for solar neutrino detection. Chapter **??** details the SNO+ detector, its detection methods and capabilities, and the upgrades from SNO to SNO+. In Chapter **??** I describe a novel theory for neutrino oscillation that modifies how neutrinos oscillate in areas of very low matter density, and gives limitations on that theory from existing measurements. Chapter **??** describes how data from the SNO+ detector was used and analyzed to measure the solar neutrino flux; Chapter **??** describes results of that analysis. Finally Chapter **??** provides summary and conclusion for this work.

Chapter 2

Overview of Relevant Physics

2.1 The Standard Model

The standard model of particle physics is our current best way of understanding all particle interactions that have so far been observed. It's defining aspect is as a gauge theory in which all interactions preserve a local $SU(3)_C \times SU(2)_L \times U(1)_Y$ symmetry, where C, L, and Y respectively indicate color, left-hand chirality and weak hyperchange. These symmetry groups specify the number of bosons that mediate each...

The $SU((3)_C$ symmetry corresponds to the strong nuclear force and quark/gluon interactions.

2.2 Neutrinos

Neutrinos were first hypothesized by Wolfgang Pauli in 1930. The motivation for the proposal the apparent violation of energy conservation in β decay (1). Several years after Pauli's speculative proposal Enrico Fermi offered a thorough model of beta decay that conserved energy using the neutrino (2). Fermi's model predicted such a small cross-section for the neutrino that some doubted it would ever be observed (3). However, roughly two decades after its initial proposal, Frederick Reines & Clyde Cowan performed an experiment that involved bombarding a tank of cadmium doped water with anti-neutrinos from nuclear reactor. Doing this they were able to observe the rate and energy of inverse β decays that occurred. The results were consistent with Fermi's model of β decay and were considered a confirmation of the neutrino's existence.

2.2.1 Neutrino Flavor

The first experimental evidence for neutrino flavor came in 1962 from an experiment (4) that studied the interactions of neutrinos that came from muon decay, and the interactions of neutrinos from beta decay. The experiment observed that neutrinos from came from muon decay would produce muons upon interacting in a detector. And neutrinos produced from β decay would create electrons in the detector. This lead to the conclusion that there are two different varieties of neutrino, the ν_e and the ν_μ, and the idea that lepton flavor is conserved. The third lepton generation, the τ and the ν_τ was discovered 13 years later in 1975 (5).

2.2.2 Neutrino Interactions

The neutrino interacts almost exclusively via the weak interaction. In principle it also interacts gravitationally and it has a non-vanishing magnetic moment so it can interact electro-magnetically, but these interaction potentials are so small they can be neglected in all practical cases (**?**). The weak interaction has a number of aspects that limit the sort of neutrino interactions that can occur. The first aspect is lepton flavor conservation, all weak interactions conserve both the total lepton number of a system, but als the total lepton flavor of the system as well. This leads to nearly all interactions involving a neutrino also involving the same flavor charged lepton. The second aspect is that the weak interaction is known to be chiral, only left-handed particles and right-handed anti-particles interact

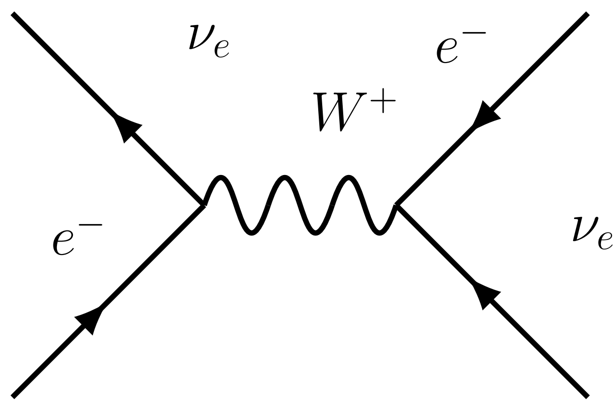

weakly. Since neutrinos only interact weakly, the only detectable varieties of neutrino is the left-handed neutrino ν^L and the right-handed anti-neutrino $\overline{\nu}^R$.

Detailed here are the neutrino interactions that are relevant to this work, a more complete overview of neutrino interactions is available in Ref (**?**).

2.2.2.1 Neutrino-Nuclear Interactions

There are two varieties of neutrino nuclear interactions that are most relevant for this work, both are coherent the charged current interaction with a neutron, and the neutral current interaction with a proton or neutron.

2.2.2.2 Neutrino-Electron Elastic Scattering

Neutrino-electron elastic scattering (ES) is an important neutrino interaction channel, for this work it is the main interaction through which neutrinos are detected. The ES process is $\nu_\mathrm{x} + e^- \to \nu_{mathrmx} + e^-$. A similar process exists for anti-neutrinos, but the focus here is on the neutrino ES interaction.

Figure **??** shows the tree level feynman diagrams for the charged current (CC) elastic scattering interaction **??** and the neutral current (NC) elastic scattering interaction **??**. The neutral current interaction is shown to involve ν_x where $x = \mathrm{e}, \mu, \tau$, and the charged current

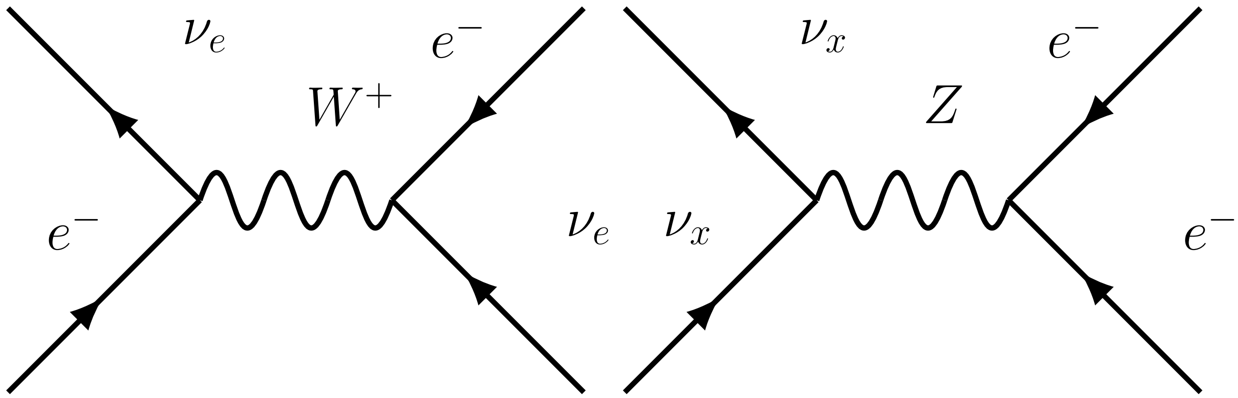

interaction involves only ν_{e}. The charged current interaction is available to neutrinos of all flavors, however, for a few reasons only the electron flavor version of the interaction is available for solar neutrinos.

The intial electron on the left hand side of the interaction is usually understood to be from an atom within target the detector, and therefore at rest within the lab frame. So the total energy in the interaction is simply $E = E_\nu + m_e$. For even the highest energy solar neutrinos $E < 20\,\mathrm{MeV}$, far less that muon rest mass of $m_\mu = 105.7\,\mathrm{MeV/c^2}$ or tau mass $m_\tau = 1776.8\,\mathrm{MeV/c^2}$. Meaning a muon or tau cannot be created; the electron with a rest mass of $m_e = 0.511\,\mathrm{MeV/c^2}$ is the only charged lepton that can be created from the CC-ES interaction for solar neutrinos. And since lepton flavor is conserved in weak interactions, the electron neutrino is the only neutrino that can produce an electron, therefore the electron neutrino is the only neutrino flavor that can undergo the charged-current elastic scattering interaction.

In practice this means that the cross section for the elastic scattering process is larger for ν_e than it is for a ν_μ or ν_τ, and the cross-section for a ν_μ is the same as that for a ν_τ.

The differential cross section of for the diagrams shown in Fig **??** can be calculated as

$$\frac{d\sigma}{dT_{\mathrm{e}}}(E_\nu,\, T_{\mathrm{e}}) = \frac{\sigma_0}{m_{\mathrm{e}}}\left[g_1^2 + g_2^2\left(1 - \frac{T_{\mathrm{e}}}{E_\nu}\right)^2 - g_1 g_2 \frac{m_{\mathrm{e}} T_{\mathrm{e}}}{E_\nu^2}\right], \tag{2.1}$$

where,

$$\sigma_0 = \frac{2G_{\mathrm{F}}^2 m_{\mathrm{e}}^2}{\pi}. \tag{2.2}$$

For $\nu_x = \nu_e$

$$g_1 = \frac{1}{2} + \sin^2\theta_{\mathrm{W}}, \tag{2.3}$$

and

$$g_2 = \sin^2\theta_{\mathrm{W}}. \tag{2.4}$$

For $\nu_x = \nu_\mu$ or $\nu_x = \nu_\tau$ g_1 and g_2 is given by,

$$g_1 = \sin^2\theta_{\mathrm{W}} - \frac{1}{2}, \tag{2.5}$$

and

$$g_2 = \sin^2\theta_{\mathrm{W}}. \tag{2.6}$$

Since the electron scattering is elastic the kinematics of the interaction leave only free parameter, the outgoing electron direction, with respect to the incoming neutrino direction, θ. For a recoil electron with a given value for θ the electron kinetic energy is given by

$$T_{\mathrm{e}} = \frac{2m_{\mathrm{e}} E_\nu^2 \cos^2\theta}{(m_{\mathrm{e}} + E_\nu)^2 - E_\nu^2 \cos^2\theta}. \tag{2.7}$$

This relationship can be used to produce the differential cross-section

$$\begin{aligned}\frac{d\sigma}{d\cos\theta} = \sigma_0 &\frac{4E_\nu^2 (m_{\mathrm{e}} + E_\nu^2)^2 \cos\theta}{[(m_{\mathrm{e}} + E_\nu^2 - E_\nu^2\cos^2\theta)]^2} \\ &\left[g_1^2 + g_2^2\left(1 - \frac{2m_{\mathrm{e}E_\nu \cos^2\theta}}{(m_{\mathrm{e}} + E_\nu)^2 - E_\nu^2\cos^2\theta}\right)^2 - g_1 g_2 \frac{2m_{\mathrm{e}^2}\cos^2\theta}{(m_{\mathrm{e}} + E_\nu)^2 - E_\nu^2\cos^2\theta}\right].\end{aligned} \tag{2.8}$$

And finally the maximum energy a recoil electron will have can be found by setting $\cos\theta = 1$ in equation (2.7), this yields

$$T_e^{\max}(E_\nu) = \frac{2E_\nu^2}{m_{\mathrm{e}} + 2E_\nu^2}. \tag{2.9}$$

Figure **??** shows the differential cross-sections for a 10 MeV neutrino. The fact that the scattering cross-section is so peaked in $\frac{d\sigma}{d\cos\theta}$ is very useufl for neutrino experiments because it means the electron direction is almost always nearly co-linear with the neutrino direction. Unforunately, since the cross-section is nearly flat in T_{e} the electron energy conveys almost no information about the incoming neutrino energy. The kinematics and cross-section of the out-going neutrino is also well predicted with respect to $\cos\theta$, however the out-going neutrino is of little interest because it in general cannot be detected.

2.2.3 Neutrino Oscillations

Neutrino oscillation is a result of the fact that neutrino flavors do not have well defined masses, instead neutrino flavor states are quantum superposition And conversely, mass states can be described as a superposition of flavor states. This can be stated more precisely as

$$|\nu_i\rangle = U_{i\ell}\,|\nu_\ell\rangle \tag{2.10}$$

Where $|\nu_\ell\rangle$ represents the neutrino flavor states, $|\nu_i\rangle$ represents the mass states, and $U_{i\ell}$ describes the mixing of these states. U is known as the Pontecorvo-Maki-Nakagawa-Sakata (PMNS) matrix, and it is exactly analogous to the Cabibbo-Kobayashi-Maskawa (CKM) matrix used to describe quark mixing. In the simplest case where the weak states and the mass states are the same U would just be the identity matrix; Under the assumption that there are three flavor states and three mass states $U_{i\ell}$ must be unitary so that the probability of observing a neutrino in any state is 1. It is known from observations of Z boson decay products that there are only three “active” neutrino flavors (**?**). Where active here means that the neutrino participates in weak interactions.

It is typical to characterize U with three angles (θ_{12}, θ_{13}, $theta_{23}$) and a complex phase δ_{cp}. Doing so allows for the SU(3) matrix to be decomposed into two SO(2) matrices and one SU(2) matrix,

$$U_{12} = \begin{bmatrix} \cos\theta_{12} & \sin\theta_{12} & 0 \\ -\sin\theta_{12} & \cos\theta_{12} & 0 \\ 0 & 0 & 0 \end{bmatrix},$$

$$U_{13} = \begin{bmatrix} \cos\theta_{13} & 0 & \sin\theta_{13}e^{-i\delta_{cp}} \\ 0 & 0 & 0 \\ -\sin\theta_{13}e^{-i\delta_{cp}} & 0 & \cos\theta_{13} \end{bmatrix},$$

$$U_{23} = \begin{bmatrix} 0 & 0 & 0 \\ 0 & \cos\theta_{23} & \sin\theta_{23} \\ 0 & -\sin\theta_{23} & \cos\theta_{23} \end{bmatrix}.$$

These matrices can be multiplied to produce the full mixing matrix $U = U_{23}U_{13}U_{12}$

The mixed nature of neutrino flavor and mass states gives rise to oscillations in the flavor content of propagating neutrinos. By definition the neutrino mass states are eigenstates of the vacuum Hamiltonian

$$H\left|\nu_i\right\rangle = E_i\left|\nu_i\right\rangle, \tag{2.11}$$

where the energy is given by the standard relativistic energy equation,

$$E_i = \sqrt{(p_i c)^2 + (m_i c^2)^2}. \tag{2.12}$$

It is typical to make the assumption that all neutrino mass states have the same momentum, $p_i = p$, and this is the assumption I'll user here as well. The equal momentum assumption allows for a straightforward derivation of the correct description of neutrino oscillations, but it is not well motivated. A thorough discussion of the assumption is available in Ref (**?**).

Applying Schrodinger's equation,

$$i\frac{d}{dt}\left|\nu_i(t)\right\rangle = H\left|\nu_i(t)\right\rangle = E_i\left|\nu_i(t)\right\rangle, \tag{2.13}$$

results in,

$$|\nu_i(t)\rangle = e^{-iE_i t} |\nu_i(t=0)\rangle \,. \tag{2.14}$$

This time evolution of mass eigenstates can be used to then describe the state of a neutrino that is created in a electron flavor eigenstate.

$$|\nu(t=0)\rangle = |\nu_e\rangle = U_{1e} |\nu_1\rangle + U_{2e} |\nu_2\rangle + U_{3e} |\nu_3\rangle = \sum_{i=1}^{3} U_{ie} |\nu_i\rangle \tag{2.15}$$

Each of the mass states' time evolution can be immediately written down from Equation (2.14),

$$|\nu(t)\rangle = \sum_{i=0}^{3} U_{ie} e^{-iE_i t} |\nu_i\rangle \,. \tag{2.16}$$

From Eq. (2.16) the quantity that's often of the most interest is the survival probability, defined as

$$P_{ee}(t) = |\langle\nu_e|\nu(t)\rangle|^2. \tag{2.17}$$

$P_{ee}(t)$ can be understood as the probability that a neutrino, produce in an electron flavor state, will be detected as an electron flavor state a time t later. The survival probability for the state given in (2.16) is

$$P_{ee}(t) = \sum_{i,j} |U_{ei}|^2 |U_{ej}|^2 e^{-i(E_i - E_j)t}. \tag{2.18}$$

It is useful to separate out the terms where $i = j$,

$$P_{ee}(t) = \sum_{i} |U_{ei}|^4 + \sum_{i,j,\, j \neq i} |U_{ei}|^2 |U_{ej}|^2 e^{-i(E_i - E_j)t}. \tag{2.19}$$

Here we can see there are terms that oscillate with time, and terms that do not.

A few more simplifications are commonly done, using the equal momentum assumption mentioned earlier and the fact the neutrino rest mass is very small, the energy differences can be simplified,

$$E_i - E_j = \sqrt{p^2 + m_i^2} - \sqrt{p^2 + m_j^2} \approx p^2 - p^2 + \frac{m_i^2}{2p} - \frac{m_j^2}{2p}. \tag{2.20}$$

To good approximation $p = E$, so

$$E_i - E_j = \frac{\Delta m_{ij}^2}{2E}, \tag{2.21}$$

where the definition of the mass-squared splittings is used,

$$\Delta m_{ij}^2 = m_i^2 - m_j^2. \tag{2.22}$$

The final simplification is to assume that the neutrino is moving very close to the speed of light, therefore any flavor oscillations over time will also occur at a distance L from the neutrino's creation. All this gives

$$P_{ee}(L, E) = \sum_{i}^{3} |U_{ei}|^4 + \sum_{i,j,\, j \neq i}^{3} |U_{ei}|^2 |U_{ej}|^2 e^{-i\left(\frac{\Delta m_{ij}^2}{2E} L\right)}. \tag{2.23}$$

Figure XXX shows this survival probability with mixing parameters matching those given in (**?**).

2.2.3.1 Matter Enhanced Oscillations

When neutrino propagate through matter this oscillation is altered. The local density of other particles modifies the vacuum Hamiltonian, adding a weak interaction potential. This interaction comes from a neutral current interaction of the form shown in $TODO$, or a flavor dependent charge current interaction with the leptons around the neutrino. Since nearly all matter contains a much higher density of electrons than the other flavors of charged lepton, the charged current reaction modifies the electron neutrino potential and not the potential for the muon or tau neutrion. The result is that the electron density through which a neutrino propagates can modify the effective mass-splitting and mixing angle for the electron neutrino. For a given neutrino energy E_ν there exists an electron density for which the effective mixing angle is maximal, this is known as the resonant density.

The masses of the neutrino mass states are not known, there are limits placed on the sum of the neutrino masses from observations of tritium decay, and from astronomical considerations.

$$H\left|\nu_i\right\rangle = m_i\left|\nu_i\right\rangle \tag{2.24}$$

2.2.4 Adabaticity

The adabiticity of neutrino oscillation refers if mass state composition of a neutrino state changes or not, if it does change then the neutrinos oscillation is non-adiabatic. A specific example is if you imagine a neutrino state that's a pure vacuum mass-1 state,

$$\left|\Psi_\nu\right\rangle = \left|\nu_1\right\rangle$$

suddenly enters a region of significant matter density where the mass states are now $\left|\nu'_k\right\rangle$. The neutrino state does not have time to evolve at all so the state does not change, but it is not longer a pure eigenstate of the mixing hamiltonian,

$$\left|\Psi_\nu\right\rangle = \left|\nu_1\right\rangle = \sum_{k=1}^{3}\left\langle\nu'_k\middle|\nu_1\right\rangle\left|\nu'_k\right\rangle .$$

Since the neutrino is no longer in a pure eigenstate the state will now oscilate.

In contrast if the neutrino slowly enters the region of significant matter density more slowly, then the neutrino state will smoothly evolve with the eigenstate, $\left|\nu_1\right\rangle \to \left|\nu'_1\right\rangle$. And so the final state of the neutrino in the adiabatic case will be,

$$\left|\Psi_\nu\right\rangle = \left|\nu'_1\right\rangle .$$

The adiabaticity of neutrino evolution will be discussed further in Chapter **??**.

2.2.5 Solar Neutrinos

Nuclear reactions in the core of the sun provide energy to maintain a equilibrium between gravitational forces and XXX forces. There exists two seperate chains of nuclear reactions that are present in typical stellar conditions, the *pp*-chain and the CNO-cycle. Figure XXX shows these two reaction chains. For the Sun the *pp* chain provides 99% of the generated nuclear energy, and the CNO-cycle provides the remaining 1%. For stars significantly more massive than the Sun, the CNO-cycle is the main energy generating mechanism.

Within the *pp*-chain there are five process that produce neutrinos. Since the Q-value the processes in the *pp* chain are all well below the rest mass of a muon or tau, the only charged lepton generated is electrons. And so from lepton flavor conservation only electron flavor neutrinos are generated. These neutrinos are produced with an energy spectrum shown in Fig. XXX.

The *hep* and ^{8}B reactions produce neutrinos with the highest energies. Since the *hep* reaction branching ratio is so low the flux of *hep* neutrinos is also very low compared to that of ^{8}B neutrinos; the *hep* flux is expected to be XXX% of the ^{8}B flux. So for water-cherenkov detectors that have a typical threshold of a few MeV, ^{8}B neutrinos are the primary source of detectable solar neutrinos.

The uncertainty on the predicted ^{8}B flux is relatively large, this comes mostly from the uncertainty on the cross-sections and how those cross-sections change with temperature, and uncertainties on the temperature profile within the core of the sun. And since the ^{8}B reaction has five preceding reactions the uncertainty on those reactions are part of the uncertainty on the ^{8}B flux.

The uncertainty on the *pp* and *pep* neutrinos is much lower for two reasons. First, because they are at early stage of the reaction chain, so their reaction rate is not dependent on any other preceding interaction. The *pp* reaction is also the main energy generating mechanism for the Sun, so measurements of the total solar luminosity provide strict constraints on the *pp* flux as well.

Neutrinos created in the solar core can experience significant mixing effects from local electron density. One of the most interesting aspects to neutrino mixing within the Sun is the MSW-effect, at a specific electron density a resonance occurs and neutrinos are maximally mixed. The condition for an MSW-resonance between any two matter states is given by

$$N_e = \frac{\Delta m^2 \cos 2\theta}{2\sqrt{2} E G_F}. \tag{2.25}$$

This condition is met for a 10 MeV at a solar radius of XXX, for the mixing parameters given in XXX For neutrinos below XXX MeV this condition is not met at any point within the sun, and so those neutrinos do not experience the MSW resonance. Once a neutrino created in the core of the sun has travelled past a solar radius of ≈XXX the solar electron density has dropped far enough that matter effects are no longer significant and neutrinos are effectively travelling through vacuum. Once in the vacuum mixing dominated region

The effect neutrino mixing has on the neutrino flux is typically summarized by the ^{8}B survival probability, $P_{ee}(E_\nu)$ over the energy range 0-15 MeV, shown in Fig **??**.

For solar neutrinos it's generally assumed that the neutrino states will evolve adiabtically. However, when the neutrino transitions through the MSW-resonance the flavor composition of the mass states changes very rapidly, so it's thought that this could lead to a non-adiabatic transition between the mass-1 and mass-2 state (**?**). For solar neutrinos the effect this transition would have on the neutrino survival probability is characterized with P_{jump},

$$P_{jump} = XXXX \tag{2.26}$$

Experimental observations of solar neutrinos so far cannot distinguish if the neutrino oscillation is fully adiabatic or not (**?**).

2.2.6 Neutrino Experiments

There's a long a diverse list of neutrino experiments that have contriubted to our current understanding of neutrinos and neutrino oscillations. I won't attempt to list them all here, but rather highlight the most immediatly relevant to this work. A more compresive review can be found in (**?**).

2.2.6.1 Homestake

The first experiment to succesfully detect solar neutrinos was the Homestake experiment. The detector was composed of approximately 100000 gallons of dry cleaning fluid. The choice of target was motivated by the high chlorine content in the cleaning fluid. Neutrinos above an energy of XXX would interact with the chlorine via beta decay, creating XXX. XXX would then decay to XXX with a half life of XXX. Periodically ^{3}He was bubbled through the target liquid to extract the atoms of XXX that had been created. Once extracted those atoms were observed with proportional counters to count the number of XXX to XXX decays. The number of observed counts was proportional to the solar neutrino interaction rate, and therefore the solar neutrino flux.

The homestake experiment ran from 1970 - 1990. The experiment was able to provide the first measurement of the solar neutrino flux above XXX MeV. In 19XX they first reported a measure flux of XXX, nearly a third of the expted rate which was XXX. This deficiency became known as the solar neutrino problem, and it was the first evidence for neutrino oscillation. The deficiency was present across the entire lifetime of the Homestake experiment, their final report flux was XXX.

2.2.6.2 SNO

The Sudbury Neutrino Observatory (SNO) is a water-cherenkov detector located roughly 2 km underground near Sudbury Ontario in Canada, it ran from $19XX$ to $20XX$. SNO was primarily a solar neutrino detector, it had the unique benefit of being able to detect neutrinos through three different interaction channels, each channel had it's own sensitivity to different flavor neutrinos. This allowed for a measurment of the ^8B solar neutrino flux that was not dependent on the flavor composition of the incoming neutrinos. This was accoplished by using a heavy-water (^2H_2O) target. Heavy-water's primary neutrino interactions are the electron scattering interaction (ES), a charged current nuclear reaction (CC), and a neutral current nuclear reaction (NC). There exists both charged current and a neutral current versions of the ES interaction; since electron neutrinos can interact through either of the two where as muon or tau neutrinos can only elastic scatter throug the neutral current version, the ES cross-section for electron neutrinos is larger than the cross-section for muon and tau neutrinos. The difference in cross-section is energy dependent, but it's roughly a factor of 6 for solar neutrino energies. The neutral current and charged current ES reactions are not treated seperately because there is no detectable signature that would allow you to discrimate between the two.

The NC interaction on a deuteron can break apart the neutron and proton that comprises the nucleus. $\nu_e + D- > p + n + \nu_e$. The free-neutron can then capture on the deuterium forming tritium (^{3}H) and emitting an XXX MeV gamma. The NC reaction has no neutrino flavor preference, so a measure of the rate of NC rate along with the process' cross-section provides a flavor independent measurement of the solar neutrino flux.

The charged current interaction on a deuteron converts a neutron to a proton and produces an electron.$\nu_e + D- > H + H + e^-$. This reaction can only occur when the charged lepton and the neutrino are the same flavor. So for typical matter this reaction only occurs for the electron flavor neutrinos, and so it provides a measurement of the electron flavor content of the solar neutrino flux.

SNO was able to seperate and count the events of each type of interaction, providing them three independent measurements of solar neutrinos. And the rates of each measurement had a different dependence on the flavor content of solar neutrinos.

2.2.6.3 Super Kamiokande

Super Kamiokande (SuperK) is a XXX kton cylindrical water cherekov detector. It started running in 19XX and has since made the most precise measurements of atmospheric neutrinos and solar neutrinos so far. It's the successor to the previous Kamiokande experiment, which was a significantly smaller and had a higher energy threshold for detection. SuperK can detect solar neutrino through only neutrino-electron elastic scattering, they do not use a D_2O target and so are not sensitive to the nuclear interactions that SNO used. Their extremely large detector volume though provides them with far more exposure than SNO could attain though. This results in a very precise measurement of the elastic scattering rate.

The SuperK experiment seperates their dataset into 4 subsets, called SuperK-I, SuperK-II, *etc*. Each dataset covers several years of data taking.

2.2.6.4 Borexino

Borexino is XXX kton spherical liquid scintillator detector. Their detector apparatus is similar to that of a water-cherenkov detector, the significant difference is that the water is replaced with pseudo-cumine, a liquid scintillator. A charged particle moving through scintillator generates rougly 50-100 times more light than a similar particle moving through just water. Water-cherenkov detector are typically limited in energy threshold and energy resolution by the number of photons produced and detected, a liquid scintillator detector solves this problem. Scintillation light, unlike cherenkov light, is isotropic and provides no information about the direction the particle was moving in.

Water-cherenkov detector are able to measure solar neutrinos by correlating the direction of detected events with the position of the sun. Since Borexino is not able to determine the direction of events within their detector, they instead perform a spectroscopic measurement. The measurement requires all sources of backgrounds to be accounted for and constrained from *ex-situ* measurements. Figure **??** shows the observed spectrum by Borexino and the spectrums of the constituent solar fluxes and backgrounds.

Borexino took data from 2007 to 2015(???), with a pause in 2010 to remove source of radioactive backgrounds and improve the radio-purity of their detector. With that data they've produced measurements of neutrino fluxes from the ^{7}Be, pep, pp, and ^{8}B; they've also placed upper limits on the flux of neutrinos from the CNO cycle and from the *hep* solar reaction. They're currently the only experiment to have measured the pp and pep neutrino fluxes.

show spectrum and table of results

2.2.6.5 KamLAND

The Kamioka Liquid Scintillator Antineutrino Detector (KamLAND) is a liquid-scintillator experiment similar to Borexino. It's primary physics goals were the detection of reactor anti-neutrinos, they are however also sensitive to solar neutrinos. Using analyses methods similar to Borexino they were able to determine the flux of 7^{Be}....

Perhaps surpising is that KamLAND's reactor neutrino measurements are in some ways more relevant to the study of solar neutrinos than their solar neutrino measurements. The long baseline and low energy of reactor neutrinos that KamLAND detects gives them unique senstivity to Δm^2_{21}. Other reactor neutrino experiments, such as Daya Bay, RENO, & Double Chooz are primarily senstive to neutrinos with too short a baseline to be strongly affected by Δm^2_{21}.

As shown in figure XXX the spectrum of reactor neutrinos that KamLAND detects is modified by an oscillatory pattern that is determined primarily by Δm^2_{21} and θ_{12}. By fitting for the amplitude and wavelength of those oscillations in the spectrum values of Δm^2_{21} and θ_{12} were determined to be The value for Δm^2_{21} is in disagreement with the value extracted by solar experiments, although it cannot be ruled out that the disagreement is a result of a statistical flucation. This discrepancy will be discussed further in sections XXX and XXX.

Chapter 3

Detector

3.1 The SNO+ Detector

The SNO+ detector can be mostly simply described as a large volume of a target material that is deep underground and is observed with an array of 9385 photomultiplier tubes (PMTs). The target material can dictaes the physical processes observable with the detector. The SNO detector was originally designed for a heavy-water (^2H_2O or D_2O) target, the benefits of a heavy-water target are discussed in Sec **??**. For SNO+ the detector will operate in three separate phases, each with a different target medium. For the entierty of the entierty of this work the target medium is light-water (H_2O); this phase is referred to as the "water phase". Following this the water is to be replaced by a liquid-scintillator, LAB-PPO (**?**), that will be the "pure scintillator phase" or just the "scintillator phase". After the scintillator phase the LAB-PPO will be doped with tellurium for a neutrinoless double-beta decay search, this is referred to as the "tellurium phase". The motivations for each phase is discussed in (**?**).

The target volume is encapsulated within a 6-meter radius spherical acrylic vessel (AV), which is held suspended in a large cavity filled with ultra-pure water (UPW). The acrylic sphere has a XXX meter acrylic chimney, called the "neck", at its top to allow access to the detector volume. Surrounding the acrylic vessel is an array of inward pointing PMTs arranged in a geodesic pattern. The structure holding these PMTs is referred to as the PMT Support Structure (PSUP). There are roughly 90 PMTs on the PSUP that point outward, toward the cavity walls. These outward facing tubes are called OWLs and are for the purpose of tagging interactions that occur outside the PSUP. There are an additional three tubes mounted at the top of the neck of the AV, these are referred to as NECK tubes.

Above the cavity volume is an optically isolated deck on which all the detector readout and trigger electronics are kept. PMTs are housed within a water-tight cassette and readout via a custom BNC-like connector that connects to the PMT interface electronics. Within the PMT housing is a custom PMT-base that fans out the approximately 2kV high voltage (HV) supply to the PMT input pins and routes the PMT return signal to the same HV supply cable.

3.1.1 Detection Mechanism

The goal of the SNO+ detector is to detect and record information about as many of the photons produced within the AV as possible. By observing photons information about the physical processes that produced the light can be inferred. Cherenkov radiation is the primary photon generating process of interest in SNO+'s water-phase. Cherenkov radiation is produced by any charged particle moving with velocity ($\vec{v}$) such that $abs\vec{v} > \frac{c}{n}$, where c is the speed of light and n is the index of refraction in the target medium (**?**).

The produced Cherenkov light has a few properties that make it a desireable method for particle detection. The first is that the number of photons produced scales nearly linearly with the energy of the particle propagating, therefore the energy of the particle can be estimated by simply counting the number of detected photons. The second desireable property is that the produced photons will be emitted in a cone, with an opening angle of approximately 42 deg with respect to the particles direction of travel. Meaning by detecting Cherenkov light the direction of travel of the initial particle can be inferred. And finally, if the time of each detected photon is well known then the requirement that all photons travel from the same point at the same speed allows the position of the particle to be deduced.

SNO+ takes advantage of each of these aspects of Cherenkov radiation to reconstruct the position, time, energy, and direction of all interacting particles in the detector. Our methods for deducing each value is detailed in Sec **??**.

For the scintillator and tellurium loaded phases scintillation processes are the dominant photon production mechanism. The Cherenkov light production is roughly the same in scintillator as it is in water, however the ratio of light produced by scintillation processes to Cherenkov light is approximately 100 : 1. With SNO+ it's not expected to be possible to infer which detected photons are from scintillation processes and which are Cherenkov radiation, so it can be treated as though all light is from scintillation. Many people are interested exploring how to separate Cherenkov light from scintillation light (**?**), and so this may be possible in the future.

The primary neutrino interaction that SNO+ is sensitive to is elastic scattering off electrons, $\nu_x + e^- \rightarrow \nu_x + e^-$ where $x = e$,μ, τ. For $x = e$ there exists a neutral current and a charged current channel, for $x = \mu$ or $x = \tau$ there exists only the neutral current channel. Nuclear interactions occur as well with the oxygen in the water, however these are rare and difficult to identify, and so are ignored typically.

The cross-section for this interaction is discussed in **??**. The forward peaked angular cross-section means that information about the neutrino direction is maintained in the interaction. But the differential cross-section for recoil energy is nearly flat below the end point. Meaning relatively little information about the incoming neutrino energy is preserved by the interaction.

The photons can the be detected by the SNO+ PMT array, and the pattern of hits analyzed to determine the electron direction, energy, and position.

SNO+ has XXX inward looking PMTs all mounted on a geodesic spere referred to as the PMT support structure (PSUP). The PMTs are at an average radius of 8.4 m from the center of the detector. Mounted on the outside of the PSUP are 90 outward looking (OWL) PMTs. These serve to reject interactions in the outer volume from cosmic muons. All PMTs are Hammatsu R1408 8-inch PMTs, which have typical quantum efficiency of $XXX\%$.

The inward looking PMTs are all housed within a plastic casette. Each PMT is also XXXcollaredXXX by an array of reflective petals which serve to increase the effective photo-sensitive area of the PMT. The reflective petals are typically referred as the PMT "concentrator". With the concetrators the geometric coverage of the PMT array is XXX, accounting for the angular acceptance of the concetrators gives an effective coverage of approximately $XXX\%$.

3.1.2 Electronics And DAQ

The hardware the connects to and reads out the PMT array forms the SNO+ data acquisition (DAQ) system. The SNO+ data acquisition (DAQ) inherit much of its design and components from SNO. There are a few notable upgrades that were made for the purpose of handling the higher light yield and event rate that SNO+ has compared to SNO. The DAQ hardware can be described as a few separate systems, the trigger system, the readout system, and the PMT interface system. The PMT interface provides an approximately 2 kV (HV) supply to each PMT and provides the signal from the PMT to the rest of the DAQ electronics. The trigger system's purpose to decide when an interesting interaction within the detector has occurred, and to start the readout process when such an interaction has occurred. The readout process is responsible for ensuring enough information about each PMT signal is recorded such that offline analysis is possible.

The first step of the PMT interface system is the PMT base. The base is responsible for fanning-out the supplied HV to the PMT dynode pins and connecting the PMT output to a PMT cable. The PMT base is housed within a water-tight cassette. The PMT cables pass through penetrations in the cavity ceiling where they then connect to the rest of the electronics. The PMT cable connects first to a PMT interface board (PMTIC). The physical connection occurs on a daughter card, called a “paddle card”, that accomadates up to eight PMT cables; Each PMTIC hosts four paddle cards. The PMTIC is responsible for fanning out the PMT high voltage to each PMT and providing channel level adjustment to the voltage each PMT receives; the voltage adjustment is done with a series of swappable resistors. The PMTIC is also responsible for separating the PMT signal from the supplied HV, this is achieved with a capacitative decoupling circuit. Once the two signals are separated the PMTIC sends the PMT signal to a front end card (FEC) via a board-to-board connector, where it enters the readout and trigger system.

That signal is compared to a threshold, if the signal is over threshold a “hit” has occurred - this threshold is often called the “channel threshold”. At the time of the channel threshold crossing the following processes occur, the name for each is given in parenthesis: a 100 ns long fixed-height square pulse is created (N100), a 20 ns fixed height square pulse is created (N20), a high gain copy of the signal is created (ESUMH), a low gain copy of the signal is created (ESUML), a linear voltage ramp begins (TAC ramp), the signal is integrated for 50 ns with high gain (QHS), the signal is integrated for up to 400 ns with high gain (QHL), and the singal is integrated for 50 ns with a low gain (QLX). These signals and values are created on a few different custom ASICs on the daughter boards. The trigger system uses the first of those 4 signals (N100, N20, ESUMH, and ESUML). The readout system uses the latter four values (TAC, QHS, QHL, QLX).

The trigger signals are all combined with their counterparts from other PMT channels across the detector, *i.e.* the N100 signals from all channels with be combined and separately all the N20 signals will be combined, *etc.* The signals are combined through analog summation, summing is done on a few different circuit boards within the detector. The FEC sums the top and bottom sixteen channels separately, the crate trigger card (CTC) sums the signals from the sixteen FECs that are in each electronics crate. The signals from each of the nineteen CTCs are all summed on the Master Trigger Card - Analog (MTCA+).

The SNO+ MTCA+ is an upgraded version of the SNO MTCAr; more information about the MTCA+ is available in Sec. 3.1.4.2.

Separate, but identical, MTCA+s are used for each of the four trigger signals. Each MTCA+ performs the analog summation with three different gains, resulting in a total of twelve signals spread across four different boards. Each of the twelve signals are separately compared to a threshold; each of the twelve thresholds are independent from each other. These thresholds are called “trigger thresholds”.

The different gains are in place due to the practical difficulty of maintaining a good signal-to-noise ratio (SNR) without limiting the range of the system. For example, if there exists 10 mV of noise in the system a 20 mV pulse would give a 2:1 SNR, however this would mean if 5000 PMT hits occurred simultaneously the signal would be 100 V in size. It is not practical to have a system with 100+ V range and 20 mV resolution, so the three different gain paths allow for three different trade-offs between SNR/resolution and range. The highest gain signal has the best SNR, but the smallest range, and so usually the highest gain signal has the lowest effective threshold. The reason being that it’s more important to have single hit resolution at a threshold of 8-hits than it is at a threshold 25 hits. The different gains on each signal are therefore labelled by their threshold (not their gain), e.g. the high, medium and low gain paths for the N100 signal are respectively called N100 Low (N100L), N100 Medium (N100M), and N100 High (N100H).

Although there are twelve signal-gain combinations available only seven are used: N100-Low, N100-Med., N100-High, N20-Low, N20-Med (also called just N20), ESUMH-Low, and ESUML-Low. Since the ESUMH and ESUML each only use one gain path, they’re usually referred to simply as ESUMH and ESUML with their gain path understood to be the high gain path.

When a trigger signal goes over its threshold a 20 ns digital pulse is emitted for that signal. This pulse is called a “raw-trigger” and there is one for each of the seven used trigger signals. The raw-trigger signals are sent from the MTCA+s to the Master Trigger

Card-Digital (MTCD). Finally, each of these seven raw-trigger signals can be masked in or masked out on the MTCD; if a raw-trigger is masked out, nothing happens when it fires, if it is masked in, then the raw trigger creates a "global-trigger" (GT) signal. That global trigger signal is fanned out to all the data crates which in turn sends the GT to all front end cards and daughter boards. As the GT signal is created the MTCD also generates a signal called Lockout (LO). Lockout is typically a 420 ns long pulse and while the signal is high the MTCD will not create any more global triggers.

Once the global trigger is created the trigger cycle is complete and the readout process begins. The raw-trigger signal that caused the global trigger, as well as any other raw-trigger signals that were high within a 20 ns window of the global trigger, are recorded and readout, this is know as the "trigger word". When the GT is created a counter, called the global trigger identifier (GTID) is incremented and readout along with the trigger word.

The four values that are created by the PMT signal crossing the channel threshold (TAC, QHS, QHL, QLX) are stored in analog memory cells on the daughter boards. They are stored for a length of time known as "GT_VALID", if a GT does not arrive before GT_VALID expires the TAC, QHS, QHL, & QLX values are discarded. A typical value for GT_VALID is 400 ns, although there exists some channel - to - channel variation. If a GT signal does arrive at the channel before GT_VALID expires the values in the memory cells are digitized and readout to a memory buffer on the FEC. The TAC ramp starts when the PMT signal crosses channel threshold and stops when the GT signal arrives at the channel. Since the TAC voltage ramp is linear over time the value of the TAC indicates when the hit occurred relative to the GT signal.

The FEC stores those values and adds information to identify which channel's data is stored, it also records the value of its own GTID. Each FEC keeps a counter that is incremented every time it recieves a global trigger signal, in princible the value of this counter will always be the same as the MTCD GTID, and the same as the counter in every other FEC in the detector. The GTID counter is our only way of associating recorded hit data with each other and with the trigger word.

In practice it's possible for a channel's GTID to become out of sync with the GTIDs of all other channels. This can result in the hits on a particular channel being associated with the wrong event. To mitigate this problem every 2^{16}th and 2^{24}th GT respectively creates a $SYNC$ and $SYNC24$ signal, those signals are sent by the MTCD to each FEC & DB. If a FEC or DB receives either of these synchronization pulses but its own GTID counter is not at an increment of 2^{16} or 2^{24} then the channel is identified as out of sync. If this happens, the GTID counter is adjusted to the correct value and the next hit to read out from the out of sync channel/channels is accompanied by a flag to indicate that it was out of sync. This system ensures a channel is never out of sync for more than 65536 events.

A short while after the data and the associated identifying information and status flags are buffered in FEC memory, the data is readout by a create level readout card, the "XL3". The XL3 is new to SNO+; it replaces the XL1 and XL2 from SNO, more will be said about the XL3 in Sec. 3.1.4.1. The XL3 reads out each FEC in sequence across the VME-like "SNOBUS" backplane. The XL3 stores data in it's own memory until eventually reading it out over ethernet to data-server process running on a near by computer.

Each data crate has its own XL3, all XL3 read out and serve data asynchronously. The data-server process receives data from each XL3 and relays that data to any clients that have subscribed to the PMT data feed. A similar process is done for the trigger word data. The MTCD sends trigger data to the data-server, the data-server relays that data to any clients that have subscribed clients.

The primary client to the data server is what's known as the "Event Builder", sometimes called the EB or just the "Builder". The Builder receieves data from the data-server and uses GTID information to associate trigger words and hits with each other. Once all the hits for an event have been associated wiht their trigger word the event has been "built" it is written to disk and the read out process for that event is complete. Data is typically taken in hour long chunks referred to as a “run”; every run has an unique number associated with it and a “run type” number that gives basic context to the detector circumstances and settings in which the data was taken. The Builder, in addition to building events, is reponsible for associating events with their run number and run type.

There are a few ancillary systems within the DAQ electronics, all of which are new to SNO+. The first is the CAEN v1720, commonly referred to as just “CAEN”, which is a 12-bit digitizer board. It’s role follows from the Analog Measurment Board (AMB) used in SNO. The CAEN is used to digitize and readout the trigger signals. It has eight available input channels that it can digitize, however, typically only three signals are actually used, those channels digitize ESUMH, N20L, and N100L. The CAEN’s digitization window and sampling rate can be varied, most commonly the digitization window is 420 ns and the sample width is 4 ns. The CAEN receives a copy of the global trigger allowing and it keeps it’s own GTID counter so its data can later be associated with the appropriate hit and trigger data. It also receives a copy of the SYNC and SYNC24 signal so it’s synchronization can be ensured.

The input voltage range for the CAEN is an adjustable 2 V window. The voltage range for the trigger signals is 10 V. The difference in ranges necessitates some way of reducing the range of the trigger signals before they’re sent to the CAEN. The simplest way of reducing the voltage range is to use a voltage divider to attenuate the signal by a factor of 5. Attenuation has a few undesirable effects though. The full range of the trigger signal is 10 V, but the vast majority of events will only use a small fraction of that range. So for events that use a small amount of the available 10 V a factor of 5 attenuation will make the signal much small than it needs to be, resulting in loss of information because the signal will be smaller than the analog noise, or from the noise digitization process itself. And for the purpose of most analyses that use the data from the CAEN it’s more important to be able to resolve a single hit than to resolve the height of the full pulse if the pulse is very large.

So a different scheme was put in place for fitting the trigger signal into the CAEN's available range. The trigger signal is clipped within the first 2 V, thereby retaining full resolution for small signals, but losing resolution for signals that go over 2 V. The board that was created to perform this dynamic range reduction was designed to optionally clip the signal or attenuate it, but for the vast majority of data taking the signal was clipped.

The board that was designed, in part, for this purpose is the Trigger Utility Board Mark - II (TUBII). Beyond modifying the trigger signals for the CAEN TUBII plays a significant role as part of the trigger and data readout systems as well. It's significance comes primarily from the fact that it acts as an auxiliary digital trigger board. It can receive raw-trigger pulses from the MTCA+s and apply customizable trigger logic to them and emit it's own raw-trigger pulses which are sent to the MTCD. TUBII also receives the global trigger signal and produces its own trigger word based upon which raw trigger pulses it had received. The TUBII trigger word is synchronized with the rest of the data for each event through it's own global trigger counter and through the SYNC/SYNC24 signals. More information about TUBII's role in the DAQ can be found in Sec. 3.1.4.4

3.1.3 Features of the SNO DAQ

There are a few aspects to the SNO and SNO+ trigger and DAQ system that are worth highlighting, as they motivate some of the work discussed in future sections.

The first of these is the unstable analog trigger baseline. TODO: Discuss here issues such as dropout, baseline shifts, and orphans.

3.1.4 Electronics Upgrades

As previously mentioned, in the scintillator and tellurium loaded phases the amount of light produced by any interaction is expected to be roughly a factor of 100 greater than the light that would be produced by water target. This increase in photon production translates to an equivalent increase in the current in the trigger sysytem and the necessary data readout rate. Additionally, since 1990's, when the SNO DAQ system was designed, the availability and sophistication of commercial computing and DAQ hardware has increased dramatically. To accomodate the increased current and data volume and to take advantage of modern hardware a few key pieces of the SNO DAQ was upgraded as part of the change from SNO to SNO+.

3.1.4.1 XL3

The SNO system used a centralized serial readout system, where each crate of electronics was readout in sequence. As part of the electronics upgrade from SNO to SNO+ this system was changed to an asynchronous, parallel readout system. The board responsible for this is the XL3 which hosts a Xilinx ML403 Evaluation platform. The ML403 uses a Xilinx Vertex-4 FPGA as its primary logic chip and has 64-MB of supporting SDRAM and persitent memory provided by a CompactFlash card reader. The XL3 & ML403 interface with the FECs in a crate through VME-like communication accross the SNOBUS backplane.

3.1.4.2 MTCA+

The SNO MTCA was not expected to be able to operate stably at the expected hit rate and occupancy of SNO+. For this reason the MTCA+ was developed, it performs the analog multiplicity sum using a series of operational amplifiers. The gain of the three different analog

One of the most transformitive changes that the MTCA+ introduces into the SNO+ trigger system is its baseline restoration circuitry. The baseline of the each trigger signal is the voltage observed when there are zero hits in the analog sum. The baselines are sensitive to a number of known factors such as the ambient temperature, the PMT noise environment, and settings on the front-end. There are also a number of factors that effect that are more difficult to identify, such as transistors on the CTC performing poorly due to age or other unknown factors. These factors lead to the baseline for any trigger signal varying by upto a few hits over the course of a few hours.

In SNO this sort of variation in the baseline could be tolerated because the threshold was far from the baseline, so variations of a few hits did not have a very large effect. In SNO+, due to many of the upgrades, a significantly lower threshold was achieved, so a variation a few hits causes a much larger change in the trigger rate, which can be higher than the maximum possible readout rate.

The MTCA+ provides two ways to mitigate baseline variations. The first is that the MTCA+ provides a relay to dynamically enable or disable each crates participation in the trigger sum. This is useful when a CTC fails, its trigger sums can be disabled to prevent it from pulling up/down the entire trigger sum to the point that stable triggering is no longer possible.

The second is baseline resotoration circuit on the MTCA+. At the final stage of each analog sum the output sum is fed through a long-pass filter to extract the average voltage over an $\approx$1 s period. That voltage is buffered and fed back into the non-inverting input of the operational amplifier used for the final stage of the of the analog sum. The effect of this feedback loop is to subtract any long term voltage offsets from the trigger sum.

Using the long term average of the trigger sum is a good way of determining the sum baseline in the limit that variations from PMT hits have a small effect on the average. Since the average is performed over a period of $\approx$1 s and the trigger signals are $\approx$100 ns wide, then a hit rate of $\approx 10^7$ hits/second is required for a significant effect on the average trigger signal. Since there are $\approx 10^4$ PMTs participating in the trigger sum at any time, and each has a typical dark rate of $\approx$ 1 kHz, the criteria of 10^7 hits/second is met. This means the baseline will be adjusted to account for the dark-rate hits. The PMT dark rate is the dominant source of hits for the detector when it has a water target, it's suspected, but not known, that this will still be true for a scintillator target as well.

Since typical variations in the baseline from thermal and other environmental effects occur on the $\approx$ 1 hour timescale the 1 s time scale for the baseline restoration provides adequate correction for those sort of effects.

3.1.4.3 Dropout

There exists one other significant source of variation for the trigger baseline, typically called "dropout". Dropout comes from a error in the design of one of the ASICs on the DB; the error results in the N100 and N20 trigger pulses from a channel being much longer than they should be, *e.g.* 1 ms wide instead of 100 ns. Since the width of the pulse is then $\approx 10^-3$ if the rate of dropout is less than $\approx$ 1 kHz, then dropout will not effect the applied baseline correction significantly. But for almost any non-zero rate of dropout the trigger itself will be effected; a single channel dropping out can be thought of as lowering effective threshold by a single hit. So dropout effects our ability to predict which events will or will not trigger our detector.

Since dropout is the result of a design error in the trigger system, the readout system is not sensitive to it, so there is no straight forward way of measuring how many or which channels are dropped out at any time. Using the data recorded by the CAEN I was able to develop a method for determining how many channels are dropped out during certain triggered events. Using that measurement I was able to estimate the rate of channels dropping out in the detector as a whole. This information is included in our simulation of the detector DAQ system to improve our model of the detector response. More will be said about the trigger and DAQ simulation in Sec.**??**.

I developed a method for extracting the dropout from the CAEN data recorded by the detector. The method is to measure the baseline of the CAEN recorded N100-Lo and N20-Lo trigger signals. The measured baseline is histogrammed and then the function

$$Pr(x) = \sum_{k=0}^{\infty} Pr(x|k)Pr(k) = \sum_{k=0}^{\infty} \frac{1}{\sqrt{2\pi\sigma^2}} e^{-\frac{(x-(S*k+C))^2}{2\sigma^2}} e^{-\lambda}\frac{\lambda^k}{k!} \tag{3.1}$$

is fit to the histogram. Eqn. 3.1 describes a series of Gaussians distributions each with width σ and separation S, and an overall shift C. The normalization of the k^{th} Gaussian is given by the value of the Poisson distribution for an average rate λ. The parameter λ corresponds the average dropout for the detector, all other parameters are treated as nuisance parameters.

Figure XXXa and XXXb show the measured dropout for two different runs, between the two runs the channel thresholds were raised across the detector. This shows that a lower channel threshold can cause a significant change in the rate of dropout. It also shows that model can match data from the detector well for high and low amounts of dropout.

For each run a dropout measurement is performed, the resulting dropout rate is later used in simulation as part of the DAQ simulation. As shown in Fig **??**, the accurate dropout simulation improves agreement between simulation and recorded data.

3.1.4.4 TUBII

TUBII is used as interface board for some of the detector calibration systems. These systems emit light into the detector and usually need to be synchronized with the trigger system. This synchronization requires a variety of pulses and delays to be tuned to account for the time it takes for signals and light propagate throughout the detector and DAQ system; TUBII provides those pulses and delays.

TUBII's customizable complex trigger logic allows it to create trigger pulses from its inputs. The input trigger signals are fed into a Xilinx MicroZed, which is an FPGA and micro-controller. The MicroZed allows for nearly any logical combination of trigger signals including using recent trigger signals to inform the current trigger logic.

Something like this is desirable for identifying and ensuring the detector will be sensitive to time correlated events. An example of this would be that the decay chain of Bi214 $\rightarrow$ Po214 $\rightarrow$ Pb212, this decay chain is referred to as BiPo214. The signature of this decay is an electron from β decay, followed, with a half life of $4\,\mu$s, by an α decay. It's very important that the α decay is detected so that the β-α decays can be identified as likely from a BiPo. If the α is not observed the β can be mis-identified and potentially leak into a signal region. TUBII is able to mitigate this risk by having a trigger that is particularly sensitive to the initial β decay and can trigger off a lower threshold input for a short time after the β trigger; ensuring that the α is detected.

TUBII also provides general purpose and "glue" functionality, facilitating different circuits from different boards in the DAQ to communicate. An example of this is that the CAEN requires the global trigger and other synchronization pulses be sent to it using Low-Voltage Differential Signaling (LVDS), but the global trigger is created using Emitter Coupled Logic (ECL). And so TUBII provides translation between these two digital signaling protocols, allowing the CAEN to remain synchronized. TUBII also accepts analog signal and can apply an MTCA - like threshold discrimination and it contains logic for creating raw-trigger pulses the same as the MTCA+.

3.1.5 Electronics Calibration

There are three primary calibrations performed for electronics to ensure that the detector behaves in a predictable way and that readout values can be interpreted for a physics analysis. The first calibration is the ECAL (Electronics Calibration), the next is the ECA (also Electronics Calibration), and the final one is the PCA (PMT Calibration).

Both the ECA and ECAL use the PEDESTAL and PULSE_GT signals. Both signals are produced on the MTCD by a pulser. The PULSE_GT simply produces GT signals at a fixed rate. The PEDESTAL signal is sent to the FECs and they fake a PMT hit occurring, *i.e.* a hit occurs in the electronics regardless of if the PMT has produced a signal or not. The channels that do or do not receive the PEDESTAL can be arbitrarily chosen. Since the PEDESTAL signal does not change the PMT signal that is measured the QHS, QHL, and QLX will always read out with the same value. The same is true for the TAC, the PEDESTAL is always emitted a fixed time before the PULSE_GT signal, meaning the time between the PEDESTAL hit and the GT readout will always be the same. The time delay between the PEDESTAL and PULSE_GT can be adjusted from XXX ns to XXX ns.

The goal of an ECAL is to provide settings for each channel that will result in a uniform detector response. Put differently, the ECAL attempts to minimize channel-to-channel variation across the detector. A number of factors need to be accounted for to produce a uniform detector response for example, the slope at which the time it takes for the TAC ramp to complete, the value for the channel threshold, the length of the GT_VALID signal, *etc.* The ECAL does this through a suite of separate tests and calibrations. ECALs are only ran as needed and typically an ECAL is only need after a board within the detector is replaced or repaired.

The ECA is generally used for determining how values from the detector map to absolute physical values. There are two varieties of ECA, PDST and TSLP. The PDST ECA consists of sending many PEDESTAL signals to each channel in the detector and measuring the distribution of charge values (QHS, QHL, and QLX) from each channel. This provides a determination of which values of each charge correspond to zero PMT signal and how much those values can vary. This zero-point measurement is where the PEDESTAL signal derives its name; it measures the charge pedestal upon which the PMT signal sits, so to speak.

The TSLP calibration follows a similar procedure, but varies the delay between the PEDESTAL and PULSE_GT. The result is a precise determination of the mapping between time (in ns) and TAC value. Beyond providing a mapping between physical values and recorded values the ECA also provides information about which electronics channels are working reliably and which are not capable of producing useful data. Channels that cannot produce useful data are removed in later analysis but are typically not modified within the electronics, except in the case where they can be repaired or replaced. Both varieties of ECA are ran on an approximately weekly basis to account for variations that may occur with time in the read out values and to quickly identify when a channel becomes unreliable.

The final electronics calibration, the PCA, is the only one to make use of the PMTs. The PCA is used for identifying the charge associated with the detection of a single photon by each PMT. There exists some variation in that value from differences in the electronics and the PMTs themselves, the PCA attempts to measure those variations. For SNO+ there exists two ways of performing a PCA, the first is with a deployed light source called the "laserball". More information about the laserball can be found in Ref (**?**). The laserball is typically placed within the center of the detector and emits light isotropically. For a typical laserball PCA the amount of light emitted is very small, such that only a few PMTs detect anything in a single event; this ensures that no PMT is likely to observe more than a single photon. Data are taken this way for a long period of time so that every PMT is hit many times over many events. The data is later analyzed to extract how much charge corresponds to a single photon for each channel.

For SNO+ a similar procedure can be done using a newly installed laser/LED system mounted on the PSUP called ELLIE (Embedded Laser/LED Light Injection Entity). The ELLIE system consists of a number of fibres that project light from one side of the PSUP, across the detector, to the PMTs on the other side. The fibres are placed at a number of different positions around the PSUP. ELLIE can be used for a number of calibration purposes, including playing a similar role to the laserball for a PCA.

Chapter 4

Chameleons

The observed discrepancy in Δm^2_{21} has motivated a number of theories that modify solar neutrinos oscillation from the standard MSW-LMA hypothesis described in section XXX. Here I'll describe a few of those theories and introduce a novel theory that modifies the potential the neutrino experiences as it travels in vacuume between the Sun and Earth.

4.0.1 Non-Standard Interactions

Solar neutrino moving through the core of the sun is one of the few sources of neutrinos that experience oscillations that are significantly modified by the ambient electron density. In principible neutrino mixing could be modified by neutrino-nuclear interactions as well, however standard nuclear interactions for the neutrino are either not flavor sensitive. Or are the result of incoherent neutrino scattering, which in most cases has a much smaller cross-section than coherent or electron scattering.

But their potential sensitivity to nuclear or modified electron scattering means they can be used to probe into our understanding of how neutrinos interact with matter. If there exists neutrino-nucleus or neutrino-electron interactions that are not accounted for within the standard model those interactions could be visible in how they modify the oscillations of solar neutrinos.

It's common to parameterize these modified interactions in a general manner, without tieing it to particular theory of modified interactions. As show in figure XXX, which shows a possible survival probability curves for a modified up or down quark-neutrino interaction. . . TODO.

4.0.2 MaVaNs

It was originally proposed in XXX that the cosmological acceleron theory for dark energy might lead to a neutrino's mass being modified by the local neutrino density. This in turn can modify neutrino mixing in the core of the sun where the neutrino propagates significant distances in areas of high neutrino density.

4.0.3 Chameleons

It was proposed in XXX that the observed expansion of the universe could be explained by introducing a 5th force that is weak in areas of high matter density. Such a force would be difficult to detect in most experiments because its effects would be small compared to standard forces. But at cosmological distance scales where the matter density is near zero, the force could be much stronger. This force is referred to as a "hameleon" force, because it is affected by it's surrounding and can "blend in" to avoid detection.

It could be the case that this force couples to neutrinos such that the coupling is sensitive to either neutrino flavor, or the mass. If so it's expected that the neutrino's mixing would be modified by the prescesce of a chameleon field. And that the chameleon-modified mixing would be only significant in areas of very low matter density. Solar neutrinos would provide almost unique sensitivity to this sort of modified vacuum mixing, because they're by far the most abundant and easily detectable source of neutrinos that travel a significant distance in areas of near-zero matter density, *i.e.* between the Sun and Earth.

This idea is the phenomonlogical basis for the idea of modified vacuum mixing. To explore this idea I developed a simulation of neutrino mixing in the sun and in the vacuum. Typical calculations of the neutrino survival probability from the sun are able to take advantage of the fact that the neutrino travels adiabatically through the varying mass density of the sun. This means that the neutrino is created in a mixture of mass states, the exact composition depending on the local electron density, and the neutrino stays in that same mixture of mass states as it exits the sun. The flavor composition of each mass state however changes, meaning that the flavor composition of the neutrino state changes, even though it's mass-state composition does not. This means that practically all one needs to do is calculate the composition of mass states that corresponds to an electron type neutrino, and then calculate the flavor content of that composition in vacuum, and that flavor content tells you the survival probability and transition probability. One is able to ignore all oscillations that may occur within the sun and simply calculate quantities for when the neutrino is created and when it is detected.

This simplification is not necessarily valid depending on how the neutrino exits the sun and how quickly the modified vacuum potential becomes significant. While the matter density is low but non-zero the neutrino will experience standard vaccuum mixing. If the neutrino changes from low to zero matter density over a distance much shorter than the oscillation length of the neutrino, the transition from standard to modified vacuum mixing potential may not be adiabatic. In which case the exact state of the neutrino at the point of the transition will determine how the flavor state of the neutrino changes as it propagates.

4.1 Simulation

Two different simulation of neutrino oscillations were developed, the first does a full simulation of the neutrino state as it propagates from the Sun to a detector at Earth. Then second calculates the evolution of the mixing eigenstates for solar neutrinos, and does not simulate individual neutrinos. The goal of both simulations is to produce a solar neutrino survival probability for any given set of standard model mixing parameters and modified vacuum mixing parameters. These two simulations methods will be discusssed in greater detail in the following sections, but the reason for the two different methods is to allow for different trade-offs between detailed simulation and computational speed.

4.1.1 Neutrino Simulation

To allow for this the simulation for modified vacuum mixing simulates the full neutrino state as it propagate through the sun. The equation

$$i\frac{d\Psi}{dx} = H\Psi \tag{4.1}$$

is evaluated numerically using the Runge-Kutta method of numerical integration. This cannot be easily evaluated analytically due to the varying density in the core of the sun. The electron density profile for the sun is given in XXX, and used to estimate the matter potential at all points within the Sun.

Performing this simulation for many neutrino energies at many different starting radii gives a representation of all possible neutrino states for solar neutrinos as they exit the Sun. This "library" of possible solar neutrino states is used as input to the modified vacuum potential simulation.

The standard solar survival probability can be calculated by calcuating $|\langle\nu_e|\Psi_\nu\rangle|^2$ for each simulated neutrino and appropriatly integrating over energies and production radii. Since neutrino states are simulated by linearly sampling starting radii and logarithmically sampling neutrino energies, states must be weighted by the relevant production PDFs in energy and radius. Figure XXX shows the standard ^{8}B survival probability simulated this way.

The chameleon portion of the simulation is done by first monte-carlo sampling neutrino energies and production radii, and looking up the simulated neutrino state that corresponds to the sampled energy & production radius. The radial production PDFs for each neutrino type that are MC sampled from are given in (**?**). The neutrino energy PDFs are given by (**?**) and (**?**), however only half of all sample energies are drawn from the relevant prodcution spectra, the other half are drawn from a uniform distribution from 0 MeV to the relevant endpoint energy. This sampling method gurantees that no energy is so poorly sampled that the simulation results are not useful, but also ensure that the most well sampled energies are those most typically produced in the Sun.

Since MC sampling produces energy and production radius values that fall between bins used when producing the solar state library, the states from the closest available radius bin is used. For energy a random choice is made between the energy bins immediatly above and below the desired energy is performed, the probability of choosing either bin is dependent on how close the desired energy is to that bin. This process is repeated for 1000000 simulated neutrinos for each solar neutrino type, *e.g.* ^{8}B, *pep*, etc.

The simulation of neutrinos this way is computationally expensive. A few methods were explored for ensuring this simulation could be performed in a reasonable amount of time. The method that was used for nearly all of the results here was to perform the Runge-Kutta integration on a GPU, which each thread corresponding to a single sample in energy and production radius.

However, even using GPU acceleration the simulation is still very time consuming, a simulation of XXX energy samples and XXX production radius samples requires roughly 2000 gpu-hours. Performing this simulation as part of a fit to data would require potentially hundreds or thousands of iteration. So it is not possible to perform the full simulation in a fit.

Fortunately, by construction the solar simulation is not effected by modified vacuum potential; the main inputs to the solar simulation are the standard model mixing parameters and the solar density profile. So, standard model mixing parameters taken from KamLAND and other non-solar neutrino experiments can be used for the solar simulation.

The result of the solar simulation is the neutrino state at 5000 samples closest to the exit of the sun. Depending on the energy of the neutrino this corresponds to state the neutrino is in in the final 150 to 500 km of the Sun, this corresponds to 0.2 to 0.7% of the solar radius (R_{odot}). And the sample-to-sample distance is 30 to 100 meters. Production radii samples are XXX m from each other, meaning that the 150 to 500 km samples taken at the end of the simulation overlap with samples taken one production radius step further. This provides a useful check of the simulation, the difference between two samples which have travelled the same distance within the sun should only depend on the difference in electron density where they were produced. Figure shows that correlation. . . .

Once monte-carlo samples of neutrino states produced by the Sun is calculated, these states are used as inputs to a simulation of the modified vacuum potential. This simulation is in principle the same as the solar simulation, it simply involve evaluting Eqn. 4.1, where H now corresponds to the modified vacuum Hamiltonian. Unlike the solar simulation though the value of H is not expected to change as the neutrino propages; Equation 4.1 can be evaluated analytically between the Sun and Earth.

The final step of the calculation is to evolve the sampled neutrino states through the Earth, to the detector. This is done similarly to the simulation of neutrino propagation through the Sun. The calculation for this is done for only a "day" path through the earth and a "night" path. The "day" path simulates the neutrino only travelling through the crust of the Earth. The "night" path simulates the neutrino travelling through the Earth, including the high density "core" region. The Earth density profile is take from PREM XXXThis results in an simulation of the day-night effect for neutrino oscillation.

The final result of this chain of simulation steps is monte-carlo samples of neutrino flavor states. The survival probability can be calculated by calculating $P_{ee}(\Psi_{nu}) = |\langle \nu_e | \Psi_{nu} \rangle|^2$ for each neutrino state. Performing an average of states and binning in neutrino energy gives the survival probability as a function of energy $P_{ee}(E_\nu)$.

Since neutrino states are monte-carlo sampled to calculate $P_{ee}(E_\nu)$ each value has statistical uncertainty from the number of samples used. This problem was somewhat exacerbated by the distributions of some of the solar neutrino energy PDFs having small values in areas that are important for comparing to solar neutrino data. For example the low energy portion of the ^{8}B solar neutrino flux is very important for solar neutrino experiments, but makes up a relatively small portion of the full ^{8}B neutrino flux. To mitigate the problem of large sampling uncertainty for important regions in solar neutrino energy, energies were sampled according to a flat distribution and according to the PDFs for each solar neutrino flux. These two methods of sampling were performed in equal proportions for each flux type.

4.1.2 Neutrino State Simulation

The other method of simulation uses the same solar inputs as the Runge-Kutta integration, but instead of simulating individiual neutrino states, only the eigen-states are simulated. For each production radius and production energy within the sun the the mixing hamiltonian is diagonalized,

$$H = UMU^\dagger + A = PDP^\dagger. \tag{4.2}$$

Where D is a diagonal matrix that gives the effective mass-squared difference between the mass-states. P gives the flavor composition of the effective mass states, $|m_1\rangle$, $|m_2\rangle$, $|m_3\rangle$. The GNU Scientific Library (6) is used to diagonlize the mixing Hamiltonian.

A neutrino, produced in an electron flavor state, can be described as

$$|\nu\rangle = \sum_{k=1}^{3} \langle m_k|\nu_e\rangle\, |m_k\rangle\,. \tag{4.3}$$

. The neutrino state is then evolved adiabatically into a modified vacuum potential given by

$$H = UMU^\dagger + A_{\mathrm{vac}}. \tag{4.4}$$

The eigenstates from the modified vacuum Hamiltonian gives the neutrino mass states $|\mathrm{vac}_1\rangle$, $|\mathrm{vac}_2\rangle$, $|\mathrm{vac}_3\rangle$. So the neutrino state is now given by

$$|\nu\rangle = \sum_{k=1}^{3} \langle m_k|\nu_e\rangle \, |\mathrm{vac}_k\rangle \, . \tag{4.5}$$

In general this equation could be used to evaluate the survival probability, as is shown in Section 2.2.3. However, equation 2.23 shows that this process produces terms that oscillate as the neutrino state evolves as well as constant terms. Solar neutrino experiments are not sensitive to oscillations in the survival probability because the production of neutrinos is distributed throughout the core of the Sun, which is many neutrino oscillation lengths across. For any detected neutrino it's impossible to say where within the Sun the neutrino was produced. Meaning there's no way to estimate how many oscillation lengths any neutrino went through while traveling from the Sun to Earth, and so the oscillations are effectively averaged over.

Because solar neutrino experiments are not sensitive to oscillations in the survival probability allows for the survival probability to be approximated by only the un-oscillating terms,

$$P_{ee} = \sum_{k=1}^{3} |\langle m_k|\nu_e\rangle|^2 \Big|\langle \nu_e|vac_k\rangle^2\Big|. \tag{4.6}$$

4.2 Global Fit

To determine solar neutrino and neutrino mixing parameters that is most consistent with experimental observations, a fit is done to published experimental results. Solar neutrino results from SNO (**?**), Super Kamiokande (**?**), Borexino (**? ?**), GNO (**?**), SAGE (**?**), and Homestake (**?**) are used. Solar neutrino fluxes are constrainted by the GS98SF2 () solar model calculations. Reactor neutrino results from Daya Bay (), KamLAND (), Reno () are also used to constrain neutrino mixing parameters. Only the reactor neutrino results from KamLAND are used, though the experiment has made solar neutrino measurements as well (**? ?**). Including the KamLAND solar results is a potential improvement for the global fitting algorithm. The KamLAND solar neutrino results are, however, compatible with and less constraining than the comparable measurements made by Borexino, SNO and SuperK, so the inclusion of those measurements would not effect any fit results significantly.

The software used for evaluating experimental consistency was developed in part by Richard Bonventre (**? ?**), but was updated to include more recent solar neutrino measurements by the Borexino and Super Kamiokande experiments. The software produces the likelihood of each experimental observation for a given set of neutrino mixing parameter and solar neutrino fluxes. Best fit parameters and uncertainties are found with the Minuit gradient descent algorithm as well an MCMC algorithm.

The mixing parameters are primarily evaluated by producing a energy dependent solar survival probability curve $P_{ee}(E_{\nu}$, then modifying the expected solar neutrino event accordingly.

4.2.1 Simplified Modified Vacuum Mixing

Probing the idea of modified vacuum mixing with the simulation detailed in section XXX proved computationally difficult. So I explored simplified method for evaluating the likelihood of a modified vacuum mixing potential. The simplification was to restrict the modified mixing to be equivalent to a change in the effective value for Δm^2_{21}. The motivation being that the observed discrepancy between solar neutrino experiments and KamLAND was only in Δm^2_{21}, and not in θ_{12}.

To explore this idea one simply can use standard methods for calculating the survival probability, but modify them such that all terms are effected by the local electron density (n_e) use a different value for Δm^2_{21} than the terms that are not effected by n_e. This introduces a new parameter into the theory, $\Delta m^2_{21}\prime$, the effective mass-squared splitting the neutrino experiences in vacuum.

With this modification a fit to solar neutrino data was performed, allowing all mixing parameters to vary. If this version of modified vacuum mixing describes reality then the best fit value for the matter mass-splitting (Δm^2_{21}) should be consistent with the value determined by KamLAND. The value for the vacuum mass splitting ($\Delta m^2_{21}\prime$) has no-apriori preferred value but it would be sensible for it to be near the standard best fit value for Δm^2_{21} as determined by solar neutrino only measurements.

The fit to data was performed using a Markov-chain Monte-Carlo method to sample the likelihood space of mixing parameters as well as solar neutrino fluxes. Figure XXX shows the results of the MCMC sampling. Marginalizing over all the mixing parameters, including $\Delta m^2_{21}\prime$, gives the best fit value for Δm^2_{21} in matter and the error on it. The marginalized result is shown in Figure XXX, the preferred value for Δm^2_{21} from solar experiments is $XXX \pm XXX$, only slightly higher than the preferred value in a standard mixing formulation, XXX, but still significantly lower than the best fit KamLAND value, XXX. The tension between the solar and KamLAND values of Δm^2_{21} is at the $XXX\sigma$ level in the standard formulation, this version of modified vacuum mixing reduces that to $XXX\sigma$, at the cost of introducing a new parameter into the theory.

The improvement in agreement between solar neutrino experiments and KamLAND on the value of Δm^2_{21} is not large enough to constitue compelling evidence that this simple version of modified vacuum mixing describes reality much better than standard mixing. And so this motivates going back to a fuller description of modified vacuum mixing, that allows for a fuller description of how neutrinos might oscillate between the Sun and Earth.

Chapter 5

Signal Extraction

Solar neutrino events are monte-carlo simulated using "RAT", a Geant-4 based simulation and analysis toolkit. RAT simulates all effects after the initial interaction, including photon propagation and detection, and particle scattering. Beyond the photon and physics simulation RAT also simluates the SNO+ DAQ and trigger electronics, allowing the effects of digitization and electronics noise to be simulated.

A solar neutrino production rate is an input to the simulation. A cross-section model take from (**?**) and (**?**) is used to estimate the elastic scattering interaction rate. RAT provides an accurate model of the detector response for each interaction.

Solar neutrino events are simulated on run-by-run basis with a fixed average rate of interactions. Each run's simulation is matched to the detector trigger and daq settings for that run. To ensure adequate monte-carlo statistics the rate of solar ν_e and $\nu_{\mu,\,tau}$ interactions is artificially enhanced by a factor of XXX and XXX; the enhanced rate is later removed as a correction to the normalization of the PDFs created from the monte-carlo simulation.

θ_{sun} is defined by

$$\cos\theta_{sun} = \vec{d} \cdot \vec{d_{sun}}, \tag{5.1}$$

where $\vec{d_e}$ represents the reconstructed direction of an event and $\vec{d_{sun}}$ is the direction vector pointing from the center of the sun to the reconstructed position of the event. $\vec{d_{sun}}$ estimates the direction the neutrino was travelling when it interacted within the detector, $\vec{d_\nu}$; it is assumed the neutrino travelled directly from the center of the sun without scattering off anything while it travelled. This is a good assumption because the neutrino cross-section is small that it's very unlikely the neutrino will interact with anything before interacting in the detector. Assuming the neutrino comes from the center of the sun is a poor assumption for an individual neutrino, but averaged over many neutrinos it is a good assumption. Additionally, correcting for the radius the neutrino is produced at would only adjust the direction by at most 0.1 deg. Figure XXX shows the angle between d_{sun} and d_ν for simulated solar neutrino events.

Figure XXX shows why θ_{sun} is a useful variable for a solar neutrino analysis. By comparing the rates of events with different values for θ_{sun} one can extract a background rate and a solar rate.

5.1 Simulation

5.1.1 RAT

A monte-carlo simulation of particle interactions in the detector is used for predicting detector observables for events. The simulation pacakage used is called RAT, it is a Geant4-based simulation that contains a detector and DAQ simulation in addition to simulation of particle interactions and photon propagation.

5.1.2 Solar Neutrino Fluxes

The expected spectral shape and normalization for the solar neutrino signal is taken from the BS05(OP) standard solar model (**?**).

5.1.3 Solar Neutrino Cross-sections

The rate of solar neutrino for a given flux follows from the cross-section for interaction. The only interaction relevant for the SNO+ detector is the neutrino-electron elastic scattering interaction.

The cross-section for the elastic-scattering interaction is take from XXX. XXX Something about radiative corrections

5.1.4 Survival Probability Simulation

A simulation of the expected solar survival probability curve for any set of mixing parameters was used. The survival probability is calculated using a 3-flavor adiabatic calculation. The calculation was developed by the SNO collaboration (**?**). is used to calculate the fraction of the solar neutrino flux that arrives at Earth and interacts as a ν_e vs the fraction that is ν_μ or ν_τ.

5.2 Reconstruction

A series of reconstruction algorithms are ran over all events that pass data cleaning. These algorithms estimate the position, time, direction, and energy of the event. All events are reconstructed under the hypothesis that the PMT hits are from cherekov radiation produced by a single electron. Additionally, the reconstruction algorithms use only the hits in the prompt time window to ensure only light that travelled directly from the event origin is used. The same reconstruction algorithms are used on both simulated and detected events.

The direction ($\vec{d}$), time (t_0), and poition ($\vec{p}$) are determined by performing a likelihood fit to the time and position of PMT hits. The algorithm evaluates the likelihood of a hypothesized event position and time by calculating the time residual for each hit PMT,

$$t_{res} = t_{PMT} - t_{transit} - t_0 \tag{5.2}$$

and using a PDF for t_{res} determined from simulation, $P(t_{res})$. The position and time that minimize the quantity

$$\sum_{i=0}^{N_{PMT}} P(t_{res}) \tag{5.3}$$

is used as the event position and time. The direction is determined by evaluating θ_{PMT} for each hit where θ_{PMT} is defined by,

$$\cos\theta_{PMT} = \vec{d} \cdot (\vec{p}_{PMT} - \vec{p})\,. \tag{5.4}$$

The likelihood, $P(\theta_{PMT})$, is determined from simulation, the direction that minimizes

$$\sum_{i=0}^{N_{PMT}} P(\theta_{PMT}) \tag{5.5}$$

is used as the reconstructed event direction.

The kinetic energy of the event is determined separately using the best fit position, and time as an input. The position and time are used to determine the number of PMT hits that occurred in a prompt 18 ns window. Then the number of photons that would most likely produce that number of PMT hits is estimated using a combination of analytic calculation and monte-carlo simulation. A look up table is used to estimate the most likely electron kinetic energy that would produce the determined number of photons. This method of energy reconstruction is called “EnergyRSP”, which stands simply for Energy Response.

Figure XXX shows the residuals for fit results on MC simulated events.

5.2.1 ITR

The time residual, defined in equationeqn:tres for a PMT hit is an extremely useful quantity because in general light that travels directly from an interaction will have a very small time residual. Light that is produced by another source, or reflects off of a detector component between production and detection will have a larger time residual.

The fraction of hits that satisify

$$-4 > t_{res} < 9 \tag{5.6}$$

is known as the "In-time ratio" (ITR). The expected distrubtion in ITR for electrons is shown in figure XXX.

5.2.2 β_{14}

The quantity β_{14} is used to quantify how isotropic the hits in an event is. It is defined as

$$\beta_{14} = \sum_{j=0}^{i} \sum_{i=0}^{i=N_{PMT}} P_1(\cos(\theta_{ij})) + P_4(\cos(\theta_{ij})) \tag{5.7}$$

The quantity θ_{ij} is the angle subtended by the vectors pointing from the reconstructed position of the event to the i^{th} and j^{th} hit PMT.

The expected distribution of β_{14} for electron events within the detector volume is shown in Figure XXX.

5.3 Calibration

The accuracy of simulated events is evaluated with data taken while a radioactive source was deployed within the detector volume. For this analysis was an ^{16}N source was used. The methods and results of the ^{16}N calibration are summarized here but are described in greater detail by **??**.

The ^{16}N source was developed by SNO, it uses a commercial deuterium and tritium generator (DT-generator) to produce gaseous ^{16}N. The gas is pumped into the deployed source where it can undergo β-decay to an exciteed state of ^{16}O, the ^{16}O will then de-excite and typically emit a XXX MeV gamma particle. Higher energy gammas are emitted at a lower rate, the branching ratios for the de-excitation gammas are shown in figure XXX.

A small block of plastic scintillator, observed by a PMT, is embedded within the source cannister. The PMT detects the β from the initial $^{16}\mathrm{N} \rightarrow {}^{16}\mathrm{O}$ decay. That PMT signal is used as a tag in the detector DAQ to identify events from the deployed source.

The source position within the AV was varied in a 3-dimensional scan. A 1-dimensional scan was done along the z-axis outside the AV volume, but inside the PSUP, as well. Scanning many positions allowed for a position dependent evaluation of systematics.

5.3.1 Energy Calibration

The detector resolution σ_E and relative energy scale δ_E are determined from the ^{16}N energy spectrum. The energy spectrum is modeled by $P(T_\mathrm{e})$, the energy spectrum in electron equivalent kinetic energy, and is given by $P_\mathrm{source}(T_\mathrm{e})$ convolved with a normalized Gaussian distribution,

$$P(T_\mathrm{e}) = N \int P_\mathrm{source}(T_e) \frac{1}{\sqrt{2\pi}\sigma_E} e^{-\dfrac{((1+\delta_E)T_\mathrm{e} - T_e')^2}{2\sigma_E^2}} dT_e'. \tag{5.8}$$

$P_\mathrm{source}(T_\mathrm{e})$ represents the distribution of deposited energy in the detector from the ^{16}N source, in electron equivalent energy. Since the ^{16}N emits gammas into the detector the mapping between gamma energy and electron equivalent energy is done by finding the electron energy that can produce the same number of Cherenkov photons as each gamma; this is not a one-to-one mapping because the same electron or gamma energy will not always produce the same number of photons. The mapping is determined from simulation and is shown in figure XXX. The gamma to electron energy mapping is then applied to the simulated ^{16}N gamma energy spectrum to determine $P_\mathrm{source}(T_\mathrm{e})$.

The values for σ_E and δ_E are extracted from (5.8) by performing a fit to the reconstructed ^{16}N energy spectrum. The fit is done to both simulated ^{16}N data and to detector data, each determining their own values for σ_E and δ_E. It's worth noting that σ_E represents only the resolution provided by detector effects, resolution from effects such as photon statistics are accounted for in $P_\mathrm{source}(T_\mathrm{e})$

Values for σ_E and δ_E are extracted for data taken, or simulated, with the ^{16}N source at many position, allowing for a position dependent determination of the energy scale and resolution. Fitting to both simulated and to detected data allows for a correction to be created that can make the two datasets match better, however the data used to create the correction cannot then be used to determine systematics. So the ^{16}N data was split into two datasets, one for determining what correction should be applied to simulation, the other for extracting systematics after the correction is applied.

The data for the correction is futher divided into position bins in z and ρ, where $\rho = \sqrt{x^2 + y^2}$. The choice of binning is motivated by the symmetry of the detector, the detector is very symmetric for an interchange of x and y or $x, y \to -x, -y$. There exists, however, signficant assymetries along the z axis from the detector neck and from the rope-net along the top of the AV. The data is divided into 4-bins along the ρ direction each 200 cm long and bins of 57 cm height along the z axis. The number of bins along the z-axis varies for each slice in ρ because data was primarily taken within the AV. Figure XXX shows the fits for δ_E and σ_E in each bin for both simulated and detected events.

Variations in δ_E along z and ρ were modeled by a polynomial given by,

$$\delta_E(\rho^2, z) = A + \left[(1 + B\rho^2)(1 + Cz + Dz^2 + Ez^3) - 1\right]. \tag{5.9}$$

Values for A, B, C, D, and E are extracted from a fit to the observed spatial variation of δ_E for simulation and data and are given in table 5.1. The reconstructed energies of simulated and detected events are then corrected according to (5.9) by their respective best fit values. The energy resolution is evaluated as a function of position but no correction is determined from it.

After the correction is applied to remaining half of the calibration dataset σ_E and δ_E are determined once more as a function of position. The bin-by-bin differences in σ_E and δ_E between simulated and detected data are taken as the systematic uncertainty for those parameters, with additional fit uncertainties added in quadrature. Averaging the bin-by-bin

	A	B	C	D	E
Data	2.53e-2	1.48-e9	-5.44e-6	2.14e-9	6.49e-13
Simulation	3.33e-2	9.48e-10	3.77e-6	4.46e-10	1.43e-13

Table 5.1: Best fit values for (5.9) for simulated and detected data, determined using units of mm for z and ρ.

systematic uncertainty over the detector volume relevant for the solar analysis yields a 2.5% uncertainty on δ_E and an 11% uncertainty on σ_E.

5.3.2 Position Calibration

Similar to the energy calibration, the position reconstruction is evaluated using ^{16}N data and simulation. The difference between the source position and the reconstructed position of each event is determined and histogrammed. A fit to that distribution is performed using a model of a Gaussian distribution with exponential tails convolved with a distribution for the first gamma interaction distance. The equation for this is given by,

$$P(x) = A \cdot \left[\left(\frac{1-\alpha}{\sqrt{2\pi}\sigma} e^{-\frac{(x-\mu)^2}{2\sigma^2}} + \frac{\alpha}{2\tau} e^{-\frac{|x-\mu|}{\tau}} \right) \circledast P_\gamma(x) \right]. \tag{5.10}$$

Where μ and σ are respectively the center and width of the Gaussian, τ represents the decay rate for the exponential tails, and α represents the relative strength of the exponential vs. the Gaussian; $P_\gamma(x)$ is distribution of distance travelled by an ^{16}N gamma before it's first interaction, it is determined from a separate MC simulation. Finally A is an overall normalization to account for the number of events included in the distribution. The Gaussian and exponential portion of (5.10) represents the spread introduced by the detector and position reconstruction, the P_γ term represents the intrinsic spread in interaction positions from the source itself. Figure XXX shows an example of this distribution and fit for a central ^{16}N dataset.

	$\langle\mu\rangle$ Systematic Uncertainty (mm)
x	+16.4, -18.2
y	+22.3, -19.2
z	+38.4, -16.7

Table 5.2: Position shift systematic uncertainties

	$\langle\sigma\rangle$ Systematic Uncertainty (mm)
x	104.0
y	98.2
z	106.2

Table 5.3: Position resolution systematic uncertainties

With this scheme three types of position uncertainties are considered, a shift uncertainty, a resolution uncertainty, and a scale uncertainty. Here a position shift is the value for μ in equation (5.10) averaged over the entire detector volume, $\langle\mu\rangle$; the position shift systematic then is the difference in $\langle\mu\rangle$ from MC simulation and as determined by detector data. Rather than averaging over all source positions $\langle\mu\rangle$ is determined averaging over scans along the x, y and z axis and so a position shift for each axial direction is determined. Only source positions along each axis are used to avoid possible correlations in each direction's position shift. The resulting systematic uncertainties along each axial direction are given in table 5.2.

The position resolution systematics is evaluated in a similar way as the position shift systmatic, comparing values for σ^2 in equation (5.10) instead of μ, but otherwise following the same procedure. Table XXX gives the extracted position resolution systematics uncertainties in mm. The uncertainties are given as one-sided because a resolution uncertainty, unlike the shift uncertainty, can only be applied to MC simulation by applying addition smearing.

	Position Scale Systematic Uncertainty (%)
x	+0.91, -1.01
y	+0.92, -1.02
z	+0.91, -0.99

Table 5.4: Position scale systematic uncertainties

The final position systematic considered is the position scale uncertainty, which represents any position depended shift in μ between simulation and data. Unlike the previous two uncertainties this systematic can effect the number of events that would be predicted to fall within a volume if the events are distributed uniformly throughout space. For this reason the position scale systematic is sometimes called the fiducial volume systematic.

The position scale for simulation and data is determined by fitting the values of μ as a function of position, along each axis, with a linear function. The best fit slope for that line gives the position depedence of the position shift. The value for that shift is defined to be zero at the center of the detector. The position scale systematic can be though of as the positional divergence introduced by the MC simulation compared to the detector data. Table 5.4 gives the position scale systematic uncertainty along each axis.

5.3.3 Direction Calibration

Like position and energy, the direction reconstruction is calibrated using data from the ^{16}N source. For each ^{16}N event the direction of the gamma is estimated as co-linear with the vector from the source position to the reconstructed event position. The dot product of that vector with the reconstructed event direction is taken, this gives the value $\cos\theta$ for that event,

$$\cos\theta = \frac{\vec{p}_{\text{fit}} - \vec{p}_{\text{source}}}{|\vec{p}_{\text{fit}} - \vec{p}_{\text{source}}|} \cdot \vec{d}_{\text{fit}}. \tag{5.11}$$

A fit is then performed to the distribution of events in $\cos\theta$ using the model of a double exponential,

$$P(\cos\theta) = \alpha\beta_s \frac{e^{\beta_s(\cos\theta-1)}}{1-e^{-\beta_s}} + (1-\alpha)\beta_l \frac{e^{\beta_l(\cos\theta-1)}}{1-e^{-\beta_l}}. \tag{5.12}$$

Where β_s and β_l represent the "short" and "long" decay constants for the two exponentials, and α represents the relative strength of the short exponential vs the long one. This model was developed by the SNO experiment and is used here simply as an empirical method to parameterize the distribution of events in $\cos\theta$. It is shown in (**?**) that the systematic uncertainties on the parameters derived from (5.12) can be transformed to a shift in $\cos\theta$ given by,

$$\cos\theta' = 1 + (\cos\theta - 1)(1 + \delta_\theta), \tag{5.13}$$

where δ_θ is the relative systematic uncertainty of β_s and β_l. Transformed this way the systematic uncertainty for the direction reconstruction is given by

$$\delta_\theta = +0.08, -0.13.$$

5.3.4 Trigger Efficiecy

The trigger efficiency for this analysis is defined to be the probability that the detector will trigger on an event as a function of the number of "in-time" hits produced by that event. Here, in-time hits is the effective maximum number of hits as seen by the analog trigger system for an event. For each event the in-time nhit, $\tilde{n}_{100}$, is well estimated by the maximum number of hits in a 100 ns window within the event. Effects from the rise-time of trigger pulses and the limited band-width of the trigger system are applied as corrections to that simple estimate.

The trigger efficiecy is estimated in two different ways, using laserball data, and using nhit-monitor data. These methods disagree by a small, but non-negligible amount, the reason for the disagreement is not well known, but the differences are taken as a systematic uncertainty. Figure XXX shows the trigger efficiecy curves for nhit-monitor and laserball data.

The nhit-monitor is detector calibration process that's run periodically during standard data taking. It simply consists of sending a variable number of pedestal hits to the front-end, and then observing if the detector triggers off of those hits or not. For the entierty of the dataset only channels in crate 4 of the detector were pedestalled for the nhit-monitor. This is one reason to prefer the trigger efficiency curve provided by laserball data, the hits from the laserball are isotropic and present a much lower risk of over-sampling a small number of channeles in the detector. Although all channels in the detector are designed function identically, this is not something that is closely monitored or tested, so it could be the case that the channels on crate 4 are not represetative of the detector as a whole.

For runs taken after the detector threshold change discussed in Sec **??** all methods agree that the trigger is 100% efficient for $\tilde{n}_{100} > 10$; only events with energy significantly below the analysis threshold (discussed in Section **??**) will have a $\tilde{n}_{100} \leq 10$, and so the discrepannt estimates of the trigger efficiecy do not have any effect on the solar analysis for the second trigger period. For the first trigger period the trigger was not 100% efficient till $\tilde{n}_{100} \approx 23$, which is much closer to the analysis energy threshold, and therefore uncertainties cannot be neglected.

5.4 Blindenss

The majority of this analyses was designed with the data blinded in the relevant energy region. The data blinding was done primarily for a nucleon decay analysis (**?**) that was performed using the same dataset as this analyses, but was done for this analysis as well because both results were produced contemporaneously.

The scheme for blinding the data was to remove all events from the dataset that had an nhit between 30 and 100, this correspond to an approximate electron energy range of 4.0 to

15.0 MeV. The analyses was designed primarily using simulation and a two-week open data period, on which no blindness restrictions were imposed.

Part way through the analysis testing and design the data was partially un-blinded to allow for an initial look at the results. Blinded events that reconstructed energy between 4.5 MeV and 15.0 MeV were added into the dataset with all energy related information removed; each event was assigned the artificial energy of 10.0 MeV. With those data, plots of the distribution of event direction with respect to the sun were created and provided a check that the results were as expected. The energy cut used to select events for that plot was performed using uncalibrated energy, so it has little bearing on the results of the full analysis.

5.5 Data Selection

Events are included or removed from the dataset across three stages of selection. First entire runs are either included or removed based upon if they meet certain criteria for data quality. The events within selected runs are then rejected or approved by a set of low-level cuts that attempt to remove events caused by instrumental backgrounds and other sources of unwanted events. Within events that pass the low-level cuts, hits can be rejected from consideration if they're deemed unlikely to have originated from light within the detector. Following that analysis level cuts are applied to the reconstructed quantities for each event. The analysis cuts are designed to maximize the signal efficiency for dataset and minimize the contamination from background sources. Each of these steps are detailed below.

5.5.1 Run Selection

Runs are rejected from the dataset if they fail to meet certain criteria for data quality and detector stability. It's first required that all meta-info about a run be created and stored within the RAT Database successfully. Those tables have information about the state of the hardware and DAQ, as well as information about the run including the run type and length. This information is necessary for assessing if the run is capable of being used for a physics analysis. It's very rare for the meta-info for a run not to be generated and stored properly, so this check has a almost no effect on the dataset.

It's first required that the run type of the run be "PHYSICS", this indicates that the DAQ settings were not changed at any point in the run and no external sources of events were present, and that the thresholds for triggering were set at a level deemed sufficient for most physics analyses. Following this checks are done that require all electronics crates have high voltage on their PMTs throughout the run. It's also required that all channels that are at high voltage are capable of reading out data, and that all crates are participating in the trigger sums. A number of separate checks are performed to ensure that all necessary DAQ processes were running well throughout the run, to ensure that the data taken during the run was not interrupted by a lapse in the DAQ.

Beyond checks on the detector state and stability, a number of checks are placed on the data taken within the run. Most of these checks are placed on the rate of certain events within the detector. It's required that the ESUMH and N100L trigger rate be greater than 5Hz and that the total trigger rate be less than 7kHz. These checks ensure that the data taken during the run triggered the detector at a rate consistent with standard running, during which the typical trigger rate is near 1kHz. Similarly it's required that fewer than 15% of all events be retrigger events (events that fall within 420 ns of the previous event). At a nominal rate of 1kHz it's very unlikely for two event to be within 420 ns by chance, so a high rate of retrigger events might indicate a high level of noise in the trigger hardware. There are however events that can occur in the detector, such as followers after a cosmic muon, that can produce re-trigger events. The cut threshold is designed to allow for retriggers from natural source but still flag detector abnormalities. These checks all ensure that the data in a run is likely to be useful for a physics analysis, but are loose enough not to bias the dataset in a way that might influence results.

5.5.2 Data Cleaning

There are a number of instrumental effects that can cause an event to be recorded by the detector, these events typically have some sort of distinguishing feature or features that set them apart from events that originate from particle interactions within the detector. A number of algorithms and cuts have been designed to identify and remove these events from the dataset. These algorithms are said to “clean” the data by removing events of instrumental origin. These definition is extended to include removing hits within an event that are likely of instrumental origin as well.

The primary type of instrumental event that must be removed is “flashers” and “shark-fin” events. Both of these result from charge build-up on the PMT-base causing a spark. For a flasher event the light from the spark escapes through the PMT face and illuminates the PMTs on the other side of the detector. Flashers occur at a rate of a few per minute. A shark-fin is similar but the spark is either small enough or located in a position such that the light does not escape the PMT. In both types of events the PMT in which the spark occurs with readout a very high-charge hit, and the channels next to it on the FEC will have low-charge hits from electronic pickup. For shark-fin event no other channels will be hit, except possibly by an accidental coincidence; for a flasher hit a number of hits will occur from the light that escaped the PMT. Since the number of PMT hits that occur in a flasher event can vary significantly, anywhere between tens of hits and hundreds, they can reconstruct to a wide range of energies and possibly contaminate a signal region. Many data cleaning cuts are designed to ensure that all flasher events are identified and removed from the dataset.

Within an event hits that are deemed unlikely to have come from a photon interacting with a PMT are removed from the analysis through hit cleaning. For this analysis the only sort of hits that were removed were those identified as coming from cross-talk between adjacent channels in the detector. Hit’s from cross-talk arise from stray capacitative coupling between adjacent, or nearby, channels on a single daughter board. Typically the noise from cross-talk will only be large enough to cause a hit on adjacent channels if the original signal is relatively large. The cross-talk hits will usually be especially low in charge because they're the result of bi-polar noise, rather than a PMT signal, and the cross-talk hit will always show up after the original hit. These criteria are codified as a cut on any hits that show up within six channels from a hit that has a pedestal subtracted QHS greater than 50 ADC counts. Of those hits if it has a pedestal subtracted QHS between 10 and -30 and are between 9 and 25 ns after the high charge hit, then the hit is flagged a cross-talk hit and removed from the analysis.

Events of instrumental origin are not well modeled within our simulation, so it is not used for evaluating the efficiencies and sacrifices of data cleaning cuts. Instead a data-driven approach is used that relies primarily on calibration data from the ^{16}N source, that analysis is detailed in **??**.The basic approach is to use tagged ^{16}N events as a source of known non-instrumental events, and evaluate what fraction of the time those events are identified as instrumentals, this provides an estimate of the data-cleaning sacrifice. The results of this analysis estimated a $XXX\%$ percent signal sacrifice from data cleaning.

An estimate of the signal contamination was performed using a method developed by SNO (**?**) and applied to the dataset (**?**); the number of instrumental events leaked into the signal region was estimated to be roughly 0.5 events over the entire dataset. However, a contamination estimate is not an input to the solar analysis, so that value is not used beyond a check that the instrumental background is reduced to a acceptable level.

Each data cleaning cut is associated with a bit in a 64-bit binary value called the data cleaning word or data cleaning mask. The cuts that each event passes or fails is tracked by its data cleaning mask. For the solar analyses all events are required to pass all cuts given by the data cleaning mask `0xFB0000017FFE`. This corresponds to the following data cleaning cuts: **Zero Zero Cut**, **Crate Isotropy Cut**, **FTS Cut**, **Flahser Geo Cut**, **ITC Time Spread Cut**, **Junk Cut**, **Muon Tag**, **Neck Cut**, **Owl Cut**, **QCluster Cut**, **QvNhit Cut**, **QvT Cut**, **Ring Of Fire Cut**, **Two-Pass Muon Follower, Short**,

Polling Cut, **Retrigger Cut**, **Two-Pass Burst Cut**, **Missed Muon Follower Cut**, **Missing CAEN Data Cut**, **Ped Cut**, **Atmospheric Cut**. Of those cuts I'll detail here those that I developed, the rest are described in **??**.

5.5.2.1 Ped Cut

During normal detector operations there are a few trigger calibration tests that are periodically ran. These tests use the PEDESTAL signal to inject a certain amount of fake hits into the detector, and events with those hits are inspected to evaluate the efficiency and quality of the trigger response. It's very important that these events are clearly identified and removed from the dataset so that the fake PEDESTAL hits are not confused for a real signal. Additionally, the trigger calibration processes usually include changing settings related to the PEDESTAL signal on the FEC, there's reason to believe these sort of changes can introduce noise to the front-end. So an aggressive approach of cutting all events that are within one second of a pedestal event is used. This not only cuts events but introduces a dead time into the dataset, this deadtime is subtracted from the overall livetime.

5.5.2.2 Missed Muon Follower Cut

The missed muon follower cut was a data cleaning cut used in SNO, but I adapted it for SNO+. In SNO it was very important to identify and cut neutrons that follow after a cosmic muon event, those neutrons could fake a neutral current solar neutrino event. In SNO+ this is not as much a problem because neutron captures in water will primarily produce a 2.2 MeV gamma, which is below the analysis threshold for solar neutrinos. However, there does exist events in the dataset which are observed to follow after high-nhit, events. The origin of these events is not well understood, they could likely be instrumental, or from spallation products within the detector. Since solar neutrino events are not expected to have any time correlations with other events in the detector, a cut can be placed on the

time between events with relatively little sacrifice.
TODO....addmore

5.5.2.3 CAEN Cut

I developed a new data cleaning cut, called the "CAEN Cut", that follows from the AMB Cut from SNO. The AMB Cut attempted to remove events from flashers the dataset by requiring that the integral and peak height of the ESUMH trigger sum (as measured by the AMB) fall below some threshold value. The CAEN Cut performs a similar function, it calculates the baseline subtracted integral and peak height of the digitized ESUMH trigger signal and places a cut on those values.

The baseline value of each trace is calculated as the average value of the first 20 samples and the 65^{th} to 85^{th} samples. I chose to use two windows, one before the trigger pulse, one after the trigger pulse, to correct for any overall slope across the digitized window. The CAEN window is 104 samples long, the final 19 samples are not used because they often include a large noise pulse. The noise pulse comes from the GT pulse arriving at the front-end and generating electrical noise, it's typically called "readout noise". The readout noise makes the last ≈ 20 samples of the CAEN trace nearly useless.

The determined baseline is subtracted from the CAEN trace and the integral and maximum peak height are calculated from the samples between the two baseline windows. To pass the CAEN Cut the peak and integral must fall between an upper and lower, nhit dependent, cut cut value. The cut values are given by

$$f(n) = C\left(1 - \sigma(n)\right) + \sigma(n)\left(mn + b\right). \tag{5.14}$$

Here $\sigma(x)$ indicates a sigmoid function,

$$\sigma(x) = \frac{1}{1 + e^{\frac{-(x-x_0)}{w}}} \tag{5.15}$$

The cut values are meant to be constant value at lower nhit, and then linear with nhit above ≈ 15 nhit, the sigmoid allows for a smooth transition between those two functions; for both the upper and lower threshold the sigmoid position (x_0) and width (w) are 15 nhit and 5 nhit respectively. The constant value at lower nhit is C the slope of the line at higer nhit is given by m and the value b is required to be

$$b = \frac{C}{mx_0} \tag{5.16}$$

so that there is not discontinuity between the two cut regions. The values for these parameters are given in Table **??**.

The reason for the two cut regions is because at lower nhit the signal peak is smaller than the noise one the ESUMH signal, so the only requirement is that the peak and integral be consistent with a noise only trigger sum. At higher nhit the ESUMH signal scales linearly with nhit, each new hit adds approximately the same amount of height to the trigger pulse.

The cut parameters were determined from two calibration datasets, the first was tagged ^{16}N events. The second was a sample of $PULSE\_GT$ triggers taken during normal running. The two datasets are used to determine the cut parameters for the two different cut regions. The ^{16}N data was used to determine cut values for the higher nhit region, the $PULSE\_GT$ data was used for the lower nhit cut values.

For both regions the value of the integral or peak height that include 99% of the events at each nhit is found. Then the parameters of Eqn. 5.14 that best fit those points is determined. Then Eqn. 5.14 with the best fit upper and lower parameters to include 99% of the calibration data become the threshold values for rejecting flasher events. The 99% criteria was chosen arbitrarily to ensure that the fraction of "good" events rejected by this cut was similar to that of other data cleaning cuts. Figure **??** shows how the ESUMH CAEN trace integral is distributed in the two calibration datasets and for standard physics data taking.

5.5.3 ZeroZero Cut

The GTID for the FEC is stored in a ripple counter, it's often the case that when the bottom two bits of the counter rollover the event that gets recorded in the FEC memory gets corrupted. When this happens the builder cannot put the corrupted hits into the event correctly, and the hits will effectively be discarded. This means that event the detectors effective photon detection efficiency is lower for events that have a GTID with 00 in the bottom two bits. Rather than correct for this inefficiecy in reconstruction, events with GTID ending in 00 are discarded. This corresponds to a random pre-scale on our by a factor of $\frac{1}{256}$.

5.5.4 Crate Isotropy Cut

The Crate Isotropy Cut is designed to remove events that are isolated in one or a few electronics crates. Events originating from light within the detector are unlikely to have any preference in electronics space. However hits caused by electrical noise that was created near the electronics can show a very distinct preference for one crate. The criteria for this cut is that fraction of hits in any single is greater that 70% and that the fractions of hits within that crate are either 80% within adjacent FECs or 70% within adjacent channels.

5.5.5 Flasher Geometry Cut

5.5.6 ITC Timespread Cut

5.6 Analysis Cuts

The dataset of events passing all data cleaning cuts is further reduced by requiring all events pass cuts on reconstructed quantities. The cuts are designed to minimize the number of events in the dataset from non-solar interactions.

Necessarily, the first of these cuts is the requirement that the reconstruction fits produce to a valid position, time and energy. The reconstruction algorithm's can fail to converge if an event occurs in an optically complicated region of the detector, *e.g.* near the detector neck. The fitting algorithms rely on the assumption that the majority of the produced light will travel directly from the event vertex to PMT array. For events in optically complicated regions this assumption is not a good one. These regions modelled in simulation, so the monte-carlo simulation estimate of the efficiency of reconstruction to produce valid fits for solar neutrino events is used.

A cut, called the "trigger efficiency" cut, is placed on the number of in-time nhits in each event. This cut ensures the dataset occupies a region where the detector trigger efficiency is well understood and near 100%. This cut ensures the analysis is minimally effected by uncertainties associated with the detector's trigger. As mentioned in Sec. **??**, the detector trigger threshold were adjusted part way through data-taking. The in-time nhit cut was adjusted to account for this. For the first trigger period all events were required to have an in-time nhit greater than or equal to 23; for the second trigger period this threshold was reduced to 10. This cut is similar to an energy cut because nhit is the best energy estimator for an event. But, as discussed below, events passing the analysis energy cut are very unlikely to fail the trigger efficiency cut.

The next analysis cut is a fiducial volume (FV) cut that requires all events be within 5.3 m of the center of the detector. This cut is designed to reduce the background from radioactive decays within the AV or from the water outside the AV. For a time period in the data taking an elevated level of radioactive backgrounds was present in the upper half of the external water. During this period the FV cut was modified to require any events in the top half of the detector ($z > 0$) fall within a radius of 4.2 m, events in the bottom half of the detector were still subject to the standard 5.3 m FV cut. Figure XXX shows the expected distribution of background events from AV and external water backgrounds

Energy	FV

Table 5.5: Cuts

compared to the distribution for solar neutrino events. This more restrictive cut was in place for 13% of the dataset livetime, runs XXX to XXX.

Two event-quality cuts are further placed on events. These cuts remove events that have an ITR or β_{14} (described in Sec. 5.2.1 and Sec. sec:b14) that is inconsistent with the event originating from Cherenkov light produced by a solar neutrino event. The ITR of events is required to be greater than 55% and the β_{14} value must between -0.12 and 0.95. These cuts are similar in purpose to the data cleaning cuts, as they attempt to remove events that are produced by sources other than Cherenkov light within the detector.

The final cut analysis cut is on the reconstructed kinetic energy of each event. The energy region for this analysis is $5.0 > T_{\mathrm{e}} < 15.0$ MeV. This region is chosen to minimize contamination from atmospheric neutrino interactions, and radioactive decays within the detector. Additionally, the only solar neutrino flux that is significant across this energy range are the neutrinos from the ^{8}B solar reaction. Neutrinos from the *hep* interaction also fall within the same energy range, however their flux is expected to be much lower than that of the ^{8}B neutrino flux that their presence can be largely neglected.

In principle the lower energy threshold could be lowered or removed to increase the fraction of solar neutrino events in the dataset, however, the rate of backgrounds from radioactive decays increases rapidly at lower energies. So no additional sensitivity to the solar neutrino interaction rate would be gained with a lower energy threshold. The 5 MeV threshold was chosen as the lowest energy from which a solar signal could still be resolved.

A summary of all cuts and their criteria, where applicable, is given in Table 5.5.

5.7 Livetime

While most event selection removes individual events based upon whether they pass or fail certain criteria, some cuts remove all events that occur for a period of time before or after some criteria is met. These cuts are said to introduce a deadtime into the dataset. The most significant example of this is the muon follower data cleaning cut, which cuts all events for 30 seconds after every muon interaction in the detector. The livetime for each run is then defined as

$$t_{\text{live}} = t_{run} - t_{\text{dead}}, \tag{5.17}$$

where t_{run} is the time between the first and last valid event within a run and t_{dead} is the sum of all deadtimes introduced into that run by cuts. The livetime is used to calculate the total exposure represented by the dataset. Table XXX shows the sum of deadtimes across all runs within the dataset. For simulated events many of the effects that necessitate deadtime are not simulated, so no deadtimes are added into the simulated runs.

5.8 Analysis

Once an MC simulated dataset and a detector dataset are selected, the analysis of those events is performed. The first steps of the analysis is to bin all events in a two-dimensional histogram of reconstructed energy and $\cos\theta_{\text{sun}}$. Events are distributed across N_θ equal width bins in $\cos\theta_{\text{sun}}$ from -1 to 1and N_E bins in energy from 5.0 to 15.0 MeV. For this analysis N_θ is 40 and N_E is 6. From 5.0 to 10.0 MeV 5 bins of width 1 MeV are used and a single bin from 10.0 to 15.0 MeV is used. Simulated and detected events are placed into separate histograms.

Simulated ν_e and ν_μ events are histogrammed separately, but given different weights in their respective histogram according to the expected survival probability for each event.

The weight for a ν_e event with neutrino energy E_ν is given by,

$$w_{\mathrm{e}} = P_{\mathrm{ee}}(E_\nu), \tag{5.18}$$

and the weight for a ν_μ event is given by,

$$w_\mu = P_{\mathrm{e}\mu} = 1 - P_{\mathrm{ee}}(E_\nu). \tag{5.19}$$

Note, no specific accounting is made for the ν_τ flux, instead only a two-flavor flux is considered. This is done because a ν_μ ES interaction is indistinguishable from a ν_τ ES interaction. So for all intents and purposes within this analysis ν_μ and ν_τ are the same and refered to by just ν_μ.

As mentioned in Sec **??**the effective livetime of the solar simulations are much larger to than the livetime of the detected dataset; the simulated histograms are scaled to by $\frac{t_{live}}{t_{sim}}$ to make the effective simulated livetime match the livetime of the detector dataset. An additional scaling is done to the simulated histograms to account for the data cleaning sacrifice, this is needed because data cleaning is not applied to simulate events. The data cleaning sacrifice was determined to be 1.2%, so the simulated histograms are scaled by a factor of 0.988.

Once these scalings are applied the ν_e and ν_μ histograms respectively represent the expected distribution and event rate for the charged current and neutral current interactions in the dataset for the nominal ^{8}B solar neutrino flux used in simulation. The ν_e and ν_μ are then combined by simply adding their bin contents together to get the expected flavor independent elastic scattering interaction rate as a function of T_{e} and $\cos\theta_{\mathrm{sun}}$. Applying additional scaling to this combined histogram is done to represent a hypothesized scaling to the overall solar neutrino flux. So the rate of solar neutrino events is given by

$$R_\nu(\cos\theta_{\mathrm{sun}}, T_{\mathrm{e}}) = S\phi\,(R) \tag{5.20}$$

Equation (5.20) is modified slightly to include a parameter related to the detector angular resolution, δ_θ,

$$R_\nu(\cos\theta_{\mathrm{sun}}, T_{\mathrm{e}}) \rightarrow R_\nu(\cos\theta_{\mathrm{sun}}, T_{\mathrm{e}}, \delta_\theta). \tag{5.21}$$

This modification is discussed more in Sec **??**.

No simulation or measurements were done for the expected backgrounds for this analysis, so a simple background model is adopted. It is assumed that the direction of any background event will be uncorrelated with the position of the sun, this is what makes $\cos\theta_{\mathrm{sun}}$ such a useful variable in this analysis. The distribution of background events is given by

$$R_{\mathrm{B}}(\cos\theta_{\mathrm{sun}}, T_{\mathrm{e}}) = R_{\mathrm{B}}(T_{\mathrm{e}}) = \frac{1}{N_\theta} n_{\mathrm{B}}(T_{\mathrm{e}}) \tag{5.22}$$

Where $n_{\mathrm{b}}(T_{\mathrm{e}})$ is number of background events in the histogram energy bins corresponding to the energy T_{e}. The number of background events in each energy bin are not known *a priori* and are treated as a nuisance parameter in the remainder of the analysis.

The total expected events in each bin can be expressed by

$$R(\cos\theta_{\mathrm{sun}},\, T_{\mathrm{e}}) = R_{\mathrm{B}}(T_{\mathrm{e}}) + R_\nu(\cos\theta_{\mathrm{sun}},\, T_{\mathrm{e}},\, \delta_\theta). \tag{5.23}$$

The unknown parameters of this rate are the 6 background rates and the solar rate and δ_θ. A fit to data is performed for equation (5.23) to extract those parameters. Goodness-of-fit is evaluated using a likelihood given by

$$\begin{aligned} &\mathcal{L}(S, \mathbf{B}, \delta_\theta | \mathbf{n}, \mu_\theta, \sigma_\theta) = \\ &\qquad \mathcal{N}(\delta_\theta, \mu_\theta, \sigma_\theta) \prod_{j=0}^{N_E} \prod_{i=0}^{N_\theta} \mathrm{Pois}\left(n_{ij},\, B_j + S\, p_{ij}(\delta_\theta)\right). \end{aligned} \tag{5.24}$$

The parameters μ_θ and σ_θ are respectively the best fit and the constraint on δ_θ from the ^{16}N source analysis. $\mathrm{Pois}\,(k, \lambda)$ is the value of the Poisson distribution at the value k for a rate parameter λ.

Equation (5.24) can be modified to fit for the solar rate in individual energy bins, rather than constraining the solar rate to be the same across all energy bins. This is done by replacing the product over energy bins, $\prod_{j=0}^{N_E}$, with the selection of j = 0, 1, *etc.* Fitting for a solar rate in each bins allows for a spectral measurement of the solar neutrino flux, as opposed to a integrated flux measurment.

5.9 Systematics

Systematics associated with event reconstruction, livetime, mixing parameters, and trigger efficiency are considered for this analysis. The event reconstruction systematics are uncertainties on the energy reconstruction scale and resolution, position reconstruction resolution and scale, and the resolution of the direction reconstruction. The uncertainties on each of these values and how they were determined is discussed in Sec 5.3.

Each systematics is treated in the same, or a similar, way, to propagate their effect to the flux result. The systematics are propagated through the analysis by modifying the relevant quantities on reconstructed monte-carlo events according to the one-σ uncertainty. The PDFs that result from the modified events are used in the analysis to extract a flux result. The difference between the systematically adjusted flux result and the standard result is taken to be the one-σ systematic uncertainty. How each variable is modified, and any deviations from this process of propagating systematics is detailed below. All systematics are treated as uncorrelated, that is variables are modified according to only one systematic at a time.

5.9.1 Energy Resolution

The energy resolution uncertainty is determined primarily from the $16N$ analysis. The systematic uncertainty on the energy resolution was determined to be $\delta_\sigma = +1.8\%, -1.6\%$. To create the energy resolution systematic's modified PDFs the reconstructed energy of the

MC simulated events is mapped to a normalized Gaussian distribution with a mean value of the event's energy and a variance given by

$$\sigma^2 = \sigma_E^2 \left((1 + \delta_\sigma)^2 - 1 \right). \tag{5.25}$$

This process of mapping a single energy value to a Gaussian distribution is referred to as "smearing". Here σ_E is given by $\sqrt{E}$ to match the functional form used in the fit for the systematics, Eqn **??**. The idea behind this smearing is to compensate for the possibility that our monte-carlo simulation could have a systematically smaller energy resolution than occurs in real data. So by applying a smearing the monte-carlo energy resolution is artificially deteriorated, and the uncertainty on the resolution is accounted for. A similar process does not exists to account for the possibility that the monte-carlo simulation has a poorer energy resolution than data taken from the real detector; there's no way to "un-smear" the reconstructed MC event energy. So, to account the effect of an over-estimated energy resolution the error on the result is assumed to be symmetric. As a penalty for this assumption the larger uncertainty between the positive and negative uncertainty on the energy resolution is used.

If the smeared event passes all cuts then each energy binned

5.9.2 Energy Scale

Systematically varied PDFs for the energy scale PDF is generated by simply modifying the reconstructed kinetic energy of each event according to

$$T\prime_e = (1 + \delta_E) T_e. \tag{5.26}$$

At all points in the analysis afterwards $T\prime_e$ is used instead of T_e.

5.9.3 Fiducial Volume

Uncertainty on the fiducial volume comes primarily from systematics associated with the position reconstruction. If the position reconstruction is more likely to pull an event towards the middle of the detector in MC simulation than in data, it will result in an over prediction of the number of events that will pass the FV cut. This possibility is accounted for by shifting the reconstructed position of simulated events according to the uncertainty, the fiducial volume cut is applied to those shifted positions. Shifting the events results in modified PDFs, those PDFs are used in the fit for the solar event rate, the difference between the best fit value extracted with the modified PDFs and the best fit value from the standard PDFs is taken to be the systematic uncertainty.

5.9.4 Angular Resolution

The angular resolution uncertainty is treated differently from other uncertainties because the distribution of events in $\cos\theta_{sun}$ is directly related to the direction resolution. To minimize the impact the angular resolution has on the result it is used as one of the parameters in the fit to the $\cos\theta_{sun}$ solar neutrino distribution, and constrained by the results of the ^{16}N analysis.

The angular resolution systematic is applied using the formula given in **??**,

$$\cos\theta' = 1 + (\cos\theta - 1)(1 + \delta_\theta). \tag{5.27}$$

Where θ is the angle between the true event direction and the reconstructed event direction, and *delta* is the angular resolution systematic uncertainty. Using (5.27) has the unfortunate downside producing unphysical values for $\cos\theta'$ for values of $\cos\theta$ near -1. For values of $\cos\theta'$ below -1 the value is instead replaced with a random value drawn from a uniform distribution $[-1, 1]$ 1. The logic behind this choice is that when an event reconstructs with a direction that's nearly 180° from the correct value, then the reconstruction has likely failed to such a degree that the reconstructed values are uncorrelated with the true values, and

Parameter	Value	Uncertainty
Δm^2_{21}	$7.5? \times 10^{-5}\mathrm{MeV/c^2}$	XXX
θ_{12}	33°	XXX
θ_{13}	8.1°	XXX

Table 5.6: A summary of the mixing parameters and their uncertainties, taken from Ref (**?**).

so drawing from a uniform random distribution preserves that uncorrleated nature without adding any additional bias.

Once the systematically varied value for $\cos\theta$ is determined, the new angle needs to be transformed into a corresponding direction vector for the particle. To do this first a vector that is normal to the plane spanned by the reconstructed and true direction vector is found by taking the cross-product between those vectors,

$$\vec{v}_{\mathrm{norm}} = \vec{d}_{\mathrm{true}} \times \vec{d}_{\mathrm{recon}}. \tag{5.28}$$

Then $\vec{d}_{\mathrm{recon}}$ is rotated around $\vec{v}_{\mathrm{norm}}$ such that the rotated vector $\vec{d}'_{\mathrm{recon}}$ now has an angle of θ'. The direction $\vec{d}'_{\mathrm{recon}}$ is then used in the analysis to generate event distrubtions in $\cos\theta_{sun}$.

Following this procedure PDFs for $\cos\theta_{sun}$ are generated for many differnt values of δ_θ, producing $P(\cos\theta_{sun}, \delta_\theta)$. The constraint on δ_θ produced by the ^{16}N analysis are included in this two-dimension PDF. $P(\cos\theta_{sun}, \delta_\theta)$ is used in the remaineder of the analysis treating δ_θ as a nuisance parameter.

5.9.5 Mixing Parameters

The central values and uncertainties of the neutrino mixing parameters, Δm^2_{21}, θ_{12} and θ_{13} is taken from Ref. (**?**). The values and uncertainties for the mixing parameters are summarized in Table 5.6. A survival probability curve is generated for each of the mixing parameters shifted by their positive and negative one-sigma uncertainty. These systematically adjusted PDFs are used in the analysis replacing the standard survial probability curve to propagate the uncertainties to the flux result.

5.9.6 Trigger Efficiency

The uncertainty on the trigger efficiecy is described in Sec **??**. PDFs for $\cos\theta_{sun}$ are generated using the more pessimistic trigger efficiecy curves measured by the laserball and TELLIE. Simulated events that have an in-time nhit that is predicted by the nhit-monitor to be 100% efficient are de-weighted to match the laserball/TELLIE efficiecy measurement.. The PDFs that result from the de-weighted events are used as the systematically adjusted PDFs to account propagate the trigger efficiecy uncertainty to the flux result.

5.9.7 Livetime

Uncertainty on the livetime comes primarily from orphaned events in the detector. Orphaned detector events are disucssed in Sec. **??**. When an orphaned event ocurrs all information about that event is lost including the time it ocurred and. . .

5.10 Results

Figure **??** shows the distribution of events in $\cos\theta_{\mathrm{sun}}$ for events over the entire energy range of 5 to 15 MeV and the fit to that distribution. The fit gives a solar event rate of 1.30 ± 0.18 events/kt-day and background rate of 10.23 ± 0.38 events/kt-day. Performing a similar fit in each individual energy bin yielded a best fit solar flux as a function of energy. The fits were combined, in accordance with Eq. 5.24, yielding an overall best fit flux of

$$\Phi_{ES} = 2.53^{+0.31}_{-0.28}(\mathrm{stat.})^{+0.13}_{-0.10}(\mathrm{syst.}) \times 10^{6}\,\mathrm{cm}^{-2}\mathrm{s}^{-1}.$$

Systematic	Effect
Energy Scale	3.9%
Fiducial Volume	2.8%
Angular Resolution	1.7%
Mixing Parameters	1.4%
Energy Resolution	0.4%
Total	5.0%

Table 5.7: Effect of each systematic uncertainty on the extracted solar neutrino flux. Systematic uncertainties with negligible effects are not shown. For asymmetric uncertainties, the larger is shown.

This value assumes the neutrino flux consists purely of electron flavor neutrinos. The result agrees with the elastic scattering flux published by Super-K, $\Phi_{ES} = (2.345 \pm 0.039) \times 10^6 cm^{-2} s^{-1}$ (**?**), combining statistical and systematic errors.

Including the effects of solar neutrino oscillations, using the neutrino mixing parameters given in Ref. (**?**) and the solar production and electron density distributions given in Ref. (**?**) gave a best fit solar flux of

$$\Phi_{^8\mathrm{B}} = 5.95^{+0.75}_{-0.71}(\mathrm{stat.})^{+0.28}_{-0.30}(\mathrm{syst.}) \times 10^6 \mathrm{cm}^{-2}\mathrm{s}^{-1}.$$

This result is consistent with the ^{8}B flux as measured by the SNO experiment, $\Phi_{^8\mathrm{B}} = (5.25 \pm 0.20) \times 10^6 cm^{-2} s^1$ (**?**), combining statistical and systematic uncertainties. Figure **??** shows the best fit solar neutrino ^{8}B event rate in each energy bin along with the predicted energy spectrum scaled to the best fit flux, and scaled to the flux measured by SNO. Each statistical error bar on the measured rate is affected by both the solar neutrino and background rates in that energy bin. Table 5.7 details how each systematic uncertainty affects this result.

Figure 5.1: Distribution of event directions with respect to solar direction for events with energy in 6.0–15.0 MeV.

The upper five energy bins, 6.0–15.0 MeV, were an extremely low background region for this analysis. There was very little background contamination from cosmogenically produced isotopes due primarily to depth of the detector. The comparatively high rate of backgrounds in the 5.0–6.0 MeV bin comes primarily from decays of radioactive isotopes, such as radon, within the detector. Figure 5.1 shows the distribution in $\cos\theta_{\mathrm{sun}}$ of events at energies above 6 MeV, illustrating the low background rate. In that energy region the best fit background rate was $0.25^{+0.09}_{-0.07}$ events/kt-day, much lower than the measured solar rate in that energy range,$1.03^{+0.13}_{-0.12}$ events/kt-day. For the region above 6 MeV, this is the lowest background elastic scattering measurement of solar neutrinos in a water Cherenkov detector.

5.10.1 Mixing Results

By using the SNO ^{8}B flux result as the true value for the full, flavor independent, ^{8}B solar neutrino flux, this measurement of the solar elastic-scattering rate can be used to the effective solar neutrino survival probability. This sort of measurement has been done before, most significantly by Super Kamiokande (**? ? ? ?**).

For any combination of electron recoil energy T_{e} and solar neutrino energy, E_{ν} the relation between the survival probability and the elastic scattering rate is........

Chapter 6

Conclusion

6.1 Wrapping up...

I rest my case.

Glossary

Roman Symbols

M Mass of object, page 79

Greek Symbols

τ Optical depth, page 79

Superscripts

* Conjugate, page 79

Subscripts

$\odot$ relating to the sun (Sol), page 79

Other Symbols

11HUGS 11 Mpc Halpha and Ultraviolet Galaxy Survey, page 79

Acronyms

2MASS Two-Micron All Sky Sruvey, page 79

References

[1] Wolfgang Pauli. **Letter to Tübingen**. 3

[2] Enrico Fermi. **Tentativo di una Teoria Dei Raggi β (Trends to a theory of β radiation)**. *Zeitschrift für Physik*, 1934. 3

[3] 3

[4] Lastname. **Title**. *Journal of Sth*, 2007. 4

[5] Lastname. **Title**. *Journal of Sth*, 2007. 4

[6] Brian Gough. *GNU Scientific Library Reference Manual - Third Edition*. Network Theory Ltd., 3rd edition, 2009. 42